JGR Space Physics

RESEARCH ARTICLE
10.1029/2019JA026892

MESSENGER Observations of Disappearing Dayside Magnetosphere Events at Mercury

J. A. Slavin[1], H. R. Middleton[2], J. M. Raines[1], Xianzhe Jia[1], J. Zhong[3], W.-J. Sun[1], S. Livi[1,4], S. M. Imber[1,5], G.-K. Poh[1,6], M. Akhavan-Tafti[1], J. M. Jasinski[1,7], G. A. DiBraccio[6], C. Dong[8], R. M. Dewey[1], and M. L. Mays[6]

[1]Department of Climate and Space Sciences and Engineering, University of Michigan, Ann Arbor, MI, USA, [2]ESA European Space and Astronomy Center, Madrid, Spain, [3]Key Laboratory of Earth and Planetary Physics, Institute of Geology and Geophysics, Chinese Academy of Sciences, Beijing, China, [4]Southwest Research Institute, San Antonio, TX, USA, [5]University of Leicester, Leicester, UK, [6]NASA Goddard Space Flight Center, Greenbelt, MD, USA, [7]Jet Propulsion Laboratory, California Institute of Technology, Pasadena, CA, USA, [8]Princeton Plasma Physics Laboratory, Princeton University, Princeton, NJ, USA

Key Points:
- The dayside magnetosphere of Mercury is observed to disappear at MESSENGER's orbit during some coronal mass ejection impacts
- The cause appears to be extreme solar wind compression and/or reconnection-driven erosion of Mercury's dayside magnetic field
- The low altitude of the bow shock during these events strongly suggests that Mercury's dayside surface experiences direct solar wind impact

Supporting Information:
- Supporting Information S1

Correspondence to:
J. A. Slavin,
jaslavin@umich.edu

Citation:
Slavin, J. A., Middleton, H. R., Raines, J. M., Jia, X., Zhong, J., Sun, W.-J., et al (2019). MESSENGER observations of disappearing dayside magnetosphere events at Mercury. *Journal of Geophysical Research: Space Physics*, *124*, 6613–6635. https://doi.org/10.1029/2019JA026892

Received 26 APR 2019
Accepted 16 JUN 2019
Accepted article online 23 JUN 2019
Published online 13 AUG 2019

Abstract MErcury Surface, Space ENvironment, GEochemistry, and Ranging (MESSENGER) measurements taken during passes over Mercury's dayside hemisphere indicate that on four occasions the spacecraft remained in the magnetosheath even though it reached altitudes below 300 km. During these disappearing dayside magnetosphere (DDM) events, the spacecraft did not encounter the magnetopause until it was at very high magnetic latitudes, ~66 to 80°. These DDM events stand out with respect to their extremely high solar wind dynamic pressures, P_{sw} ~140 to 290 nPa, and intense southward magnetic fields, B_z ~ −100 to −400 nT, measured in the magnetosheath. In addition, the bow shock was observed very close to the surface during these events with a subsolar altitude of ~1,200 km. It is suggested that DDM events, which are closely associated with coronal mass ejections, are due to solar wind compression and/or reconnection-driven erosion of the dayside magnetosphere. The very low altitude of the bow shock during these events strongly suggests that the solar wind impacts much of Mercury's sunlit hemisphere during these events. More study of these disappearing dayside events is required, but it is likely that solar wind sputtering of neutrals from the surface into the exosphere maximizes during these intervals.

1. Introduction

Since the initial Mariner 10 discovery of its weak, rotation-axis-aligned dipolar magnetic field (Anderson et al., 2011; Ness et al., 1974), there has been great interest in this, the smallest of the solar system's six planetary magnetospheres. The mean distance from the internal dipole to the nose of Mercury's magnetopause is only ~1.5 R_M (Slavin et al., 2009; Winslow et al., 2013; Zhong et al., 2015). As originally found by Mariner 10, the structure of Mercury's magnetosphere is quite similar in many ways to that of the Earth (e.g., Alexeev et al., 2010). However, the features of the Earth's magnetosphere that map to the interior of Mercury due to its large size relative to its magnetosphere, such as a radiation belts and Region 2 currents, are not present (Ogilvie et al., 1977; Slavin et al., 1997). Mercury's magnetic dipole is offset to the north by 0.2 R_M (1 R_M = 2,440 km; Alexeev et al., 2010; Anderson et al., 2011), which introduces significant north/south asymmetries in the polar magnetic fields, the size of the polar caps, the loss cones, and other phenomena (see review by Koth et al., 2019). Numerical simulations of the solar wind interaction with Mercury's magnetic field have reproduced much of the magnetospheric structure observed by Mariner 10 and MErcury Surface, Space ENvironment, GEochemistry, and Ranging (MESSENGER) missions (Benna et al., 2010; Dong et al., 2019; Janhunen & Kallio, 2004; Jia et al., 2015; Kabin et al., 2000; Kidder et al., 2008; Muller et al., 2012; Trávníček et al., 2009, 2010; Varela et al., 2015; Wang et al., 2010; Exner et al., 2018).

Despite the small dimensions of Mercury's dayside magnetosphere and the high solar wind pressure in the inner solar system, numerous studies have found that simple Earth-like compression of the forward magnetopause will place the magnetopause within a few proton gyroradii (where 1 gyroradius ~50 km for solar wind protons) of the surface no more than a few percent of the time (e.g., Siscoe and Christopher, 1975; Slavin & Holzer, 1979; Winslow et al., 2013; Zhong et al., 2015; Johnson et al., 2016). This conclusion was bolstered by the work of Hood and Schubert (1979) and Suess and Goldstein (1979) who first modeled the effects of induction currents driven within Mercury's interior by solar wind pressure enhancements.

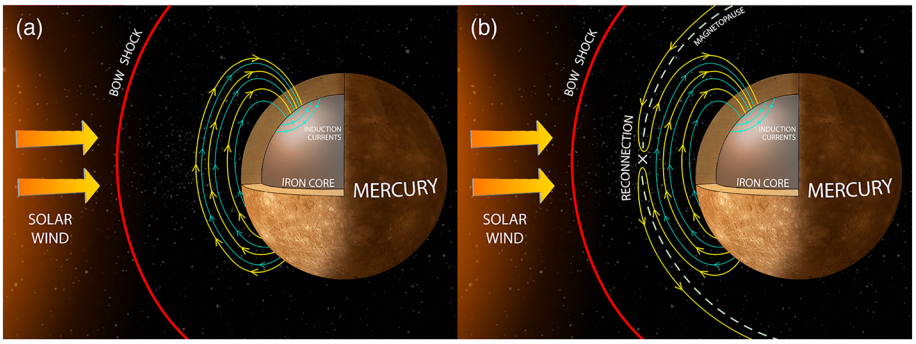

Figure 1. (a) Increases in solar wind pressure drive induction currents (green loops) at the top of Mercury's large iron core. The sense of these currents is to oppose the compression of the intrinsic magnetic field (yellow) by generating additional magnetic flux (green field lines) that, when added to the intrinsic flux due to the deep planetary dynamo, acts to balance the increased solar wind pressure. (b) Magnetic reconnection between the interplanetary magnetic field and the planetary magnetic field reduces the effectiveness of induction by removing magnetic flux from the dayside magnetosphere and transporting it to the tail (adapted from Slavin et al., 2014).

These currents are expected to flow on the surface of Mercury's ~2,000-km radius iron core (Smith et al., 2012) as shown in Figure 1a (from Slavin et al., 2014). Their results indicated that induction would "stiffen" the planetary magnetic field to the point where solar wind ram pressures of ~200 to 250 nPa would be required to compress the magnetopause to the surface (Glassmeier et al., 2007). Indeed, analysis of the most highly compressed dayside magnetosphere intervals recorded by MESSENGER has found that induction currents can increase Mercury's total magnetic moment by up to ~ 25% (Jia et al., 2019).

Figure 1a depicts this effect by coloring the closed dipolar magnetic fields in the dayside magnetosphere according to their source. The dipolar magnetic fields due to the core dynamo are yellow while the magnetic fields due to induction are green. Slavin et al. (2014) first demonstrated the effects of these induction currents on the standoff distance of the magnetopause using MESSENGER data collected during coronal mass ejections (CMEs) and high-speed streams. These interplanetary events typically bring with them sudden solar wind pressure increases of ~3 to 5 times the mean observed at Mercury. The effects of more modest changes in the solar wind pressure on induction currents as Mercury moves between its perihelion and aphelion have been well modeled by Zhong, Wan, Wei, et al. (2015) and Johnson et al. (2016).

Reconnection at the dayside magnetopause transfers magnetic flux from the closed-field-line region in the forward magnetosphere into the open-field-line lobe regions of the magnetotail as illustrated in Figure 1b. The return circulation is driven by reconnection in the cross-tail current sheet. The complete circulation of magnetic flux and plasma to the tail and back again is termed the "Dungey cycle" (Dungey, 1961). The speed of the internal plasma convection and the scale of the system determine the length of the Dungey cycle, which is 1–3 hr at Earth (e.g., Borovsky et al., 1993; Tanskanen, 2009). At Mercury, however, the time required for this cycle is only ~3 min (Siscoe et al., 1975; Slavin et al., 2010; Imber and Slavin, 2017). For this reason, Mercury's magnetosphere can move from quiescent to disturbed states on time scales of only a few minutes. This is much faster than the 30–60 min that MESSENGER spent inside Mercury's magnetosphere each orbit (see Slavin et al., 2019).

At Earth a large magnetic shear, greater than 90°, across the magnetopause is generally necessary before intense magnetic reconnection can occur (Paschmann et al., 1986; Sonnerup et al., 1990; Webster et al., 2018). These larger shears are present whenever the upstream interplanetary magnetic field (IMF) has a southward component and they increase as B_z becomes increasingly negative. Mercury's response to IMF has been found to be somewhat different from the Earth with the effects of reconnection usually being present whenever there is even a small magnetic shear across the magnetopause (DiBraccio et al., 2013; Slavin et al., 2009). Gershman et al. (2013) examined the intense draped magnetic fields in the dayside magnetosheath and argued that they are due to the low solar wind Alfvénic Mach number (M_A) conditions in the inner solar system. They found, in agreement with the theoretical arguments of Zwan and Wolf (1976), that the MESSENGER observations were consistent with the low solar wind M_A reducing the plasma heating at the bow shock and producing a low-β magnetosheath, where β is the ratio of plasma thermal

pressure to magnetic pressure. Under these conditions, the stress exerted on the subsolar magnetosheath by the solar wind is increasingly supported by the draped IMF. This, and the weak plasma heating at the low Mach number bow shock, contributes to the formation of the thick, low-β plasma depletion layer adjacent to the magnetopause that is unique Mercury's interaction with the solar wind (Zwan and Wolf, 1976; Gershman et al., 2013).

An important aspect of the thick plasma depletion layer at Mercury is that magnetopause reconnection usually involves magnetic fields that are comparable in magnitude on both sides of the current sheet, a situation that is termed "symmetric" reconnection. In contrast, "asymmetric" reconnection is the typical for the magnetopause boundary at all of the other intrinsic magnetospheres because they are located farther from the Sun where the solar wind M_A is much higher. This is an important distinction because, for comparable magnetic shear angles, symmetric reconnection is always faster than the asymmetric case due to the high Alfvén speed on both sides of the reconnecting current sheet (e.g., Sonnerup, 1974). In fact, Slavin and Holzer (1979) argued that, on average, the rate of reconnection at Mercury would be found to be greater than at Earth due to the high Alfvénic speed and low M_A conditions in the inner solar system. Further, they used the observed effects of reconnection at Earth and scaling arguments to predict that the magnetopause at Mercury would often be eroded to very low altitudes where direct solar wind impact could take place on Mercury's surface. However, the impact of induction in the interior of the planet was not considered in this early analysis.

Dayside reconnection at Mercury has broad impacts on this planet's environment because of the role of solar wind precipitation on surface sputtering and volatile desorption into its neutral exosphere (Killen et al., 2019) and the transfer of solar wind energy and plasma into this small, but extremely dynamic magnetosphere (Slavin et al., 2019). The newly opened Mercury field lines carried tailward by the solar wind all map to the north or south magnetospheric cusps and pivot about the cusps as the high-altitude end is incorporated into the tail lobes. These tail magnetic fields that have recently been added to the outer layers of the tail lobes then convect equatorward toward the cross-tail current sheet. Solar wind particles generally have a significant component of their velocity parallel to the interplanetary magnetic field. Following reconnection between the IMF and the planetary magnetic field, many of these solar wind particles are channeled inward toward the planetary surface where they will impact unless mirroring takes place first (Jasinski et al., 2017; Raines et al., 2014). Cusp magnetic flux tubes within which the magnetic field is depressed due to the diamagnetism of the plasma injected by reconnection at the magnetopause are known as cusp plasma filaments (Slavin et al., 2014). Detailed analyses by Poh et al. (2016) have shown that it is very likely that these filaments are the low-altitude extensions of flux transfer events. They have been shown to magnetically map down to the surface foot print of the cusp where they contribute significantly to particle precipitation in Mercury's cusp region (Poh et al., 2016). The discovery of these cusp plasma filaments strongly supports the hypothesis that Mercury's magnetospheric cusps are primary sites for solar wind impact on Mercury's surface with the southern cusp being larger in area due to the northward offset of the planetary dipole (Massetti et al., 2003; Korth et al., 2019). The direct impact of solar wind protons not only sputters neutral atoms into Mercury's exosphere (e.g., Pfleger et al., 2015) but also sputters ions into the high-latitude magnetotail where they mix with solar wind that mirrored at low altitudes to form the plasma mantle (DiBraccio et al., 2015; Jasinski et al., 2017). This impact of solar wind plasma beneath the cusps also contributes to space weathering of the surface (Domingue et al., 2014; Pfleger et al., 2015).

In this study, we examine four low-altitude MESSENGER passes over the dayside hemisphere of Mercury for which *no dayside magnetosphere, only magnetosheath plasma was observed*. Such events, or ones similar to them, have been noted previously by Raines et al. (2015), Zhong, Wan, Slavin, et al. (2015), Slavin et al. (2019), and Winslow et al. (2019), but not analyzed in detail beyond noting their presence in the MESSENGER data set. We term these intervals "disappearing dayside magnetosphere" (DDM) events. On these occasions magnetosheath plasma was observed as MESSENGER moved either poleward (three cases) or equatorward (one case) over the dayside hemisphere of Mercury with the magnetosphere not being entered and the magnetopause not being crossed until the spacecraft was at very high latitudes just forward of the terminator plane. Here we will show that the DDM intervals stand out with respect to their extremely high solar wind pressures, ~140 to 290 nPa, which were inferred from the analysis of the high-latitude magnetopause crossings. These very high solar wind pressures were supported by CCMC ENLIL-WSA + Cone

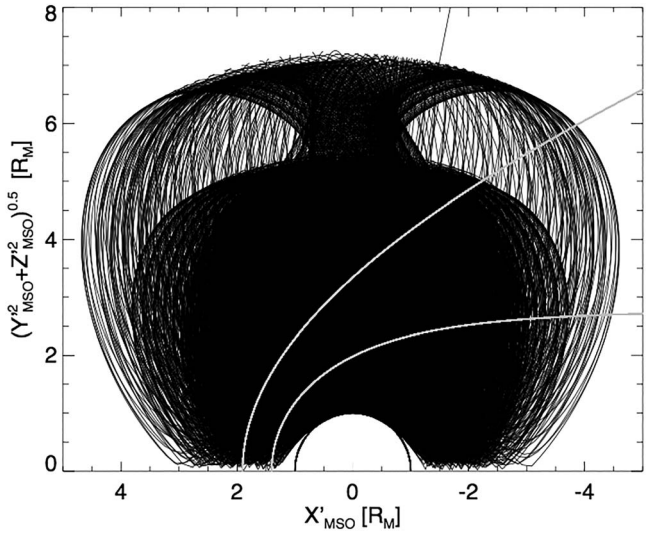

Figure 2. Every other MESSENGER orbit for its four-year mission have been plotted in solar wind aberrated, cylindrical MSO coordinates. The mean bow shock and magnetopause from the axisymmetric conic surfaces determined by Winslow et al. (2013) are displayed. Note the clear signature of the change in apoapsis altitude early in the mission and the dense coverage of the near-Mercury magnetosheath and magnetosphere (see discussion in Slavin et al., 2019).

model runs based upon CME observations by other spacecraft. We also find that intense southward magnetic fields, B_z ~ −100 to −400 nT, are present in the magnetosheath and very frequent encounters with flux transfer events (FTEs) are recorded by MESSENGER with the peak frequency occurring over the northern cusp. During these DDM events the forward bow shock was also observed to be located unusually close to the planet with a subsolar altitude of ~1,200 km, or slightly less than half of its mean position. It is suggested that these DDM events, which are all associated with CME impacts, are due to extreme solar wind compression and/or reconnection-driven erosion of the dayside magnetosphere. It is likely that the solar wind directly impacts the surface over much of Mercury's sunlit hemisphere during DDM intervals. For this reason it is probable that the maximum contribution of solar wind surface sputtering to Mercury's neutral exosphere takes place during these events.

2. MESSENGER Mission

The MESSENGER spacecraft was inserted into an ~12-hr period, 82° inclination, high eccentricity (~20 × 15,000-km altitude) orbit about Mercury on 18 March 2011 (Solomon et al., 2007). The period of the orbit was reduced on 16 April 2012 to ~8 hr by lowering the apoapsis altitude to ~10,000 km. This change in apoapsis part way through the mission resulted in rather complete sampling of Mercury's magnetosphere and its principal current systems between the nose region and ~3 to 4 R_M downstream of the center of the planet. The trajectory of the spacecraft over its approximately four years in orbit is plotted in Figure 2. Average bow shock and magnetopause surfaces (Winslow et al., 2013) are shown for comparison. The coordinates utilized are solar wind aberrated cylindrical Mercury Solar Orbital (MSO) coordinates, wherein the X_{MSO} axis points from Mercury's center toward the Sun, the Y_{MSO} axis lies in Mercury's orbital plane and it is positive in the direction opposite to planetary motion, and Z_{MSO} completes the right-handed orthogonal system. The solar wind aberration is indicated by the primes, X'_{MSO}, Y'_{MSO}, and Z'_{MSO}. The aberration has been carried out using Mercury's orbital speed as a function of distance from the Sun and rotating the MSO X and Y axes until X'_{MSO} is opposite to an assumed mean 400-km/s radial solar wind. After depleting the last of its fuel, the MESSENGER spacecraft impacted Mercury's surface on 30 April 2015 following a series of controlled low-altitude orbits.

3. Disappearing Dayside Magnetosphere Events

The strong northward magnetic field just inside the dayside magnetopause at Mercury during coronal mass ejections is due to both the deep dynamo and compression-driven currents on the surface of its large iron core (Dong et al., 2019; Hood & Schubert, 1979; Jia et al., 2015; Slavin et al., 2014). In fact even the modest change in solar wind pressure as Mercury moves from lower mean solar wind pressures at aphelion to higher at perihelion increase its total magnetic moment by ~ 5% (Johnson et al., 2016; Zhong, Wan, Wei, et al., 2015). Jia et al. (2019) surveyed MESSENGER's four-year data set and identified eight passes through Mercury's dayside magnetosphere for which the magnetic field just inside of the magnetopause exceeded 300 nT. The upstream solar wind ram pressures were estimated to range from ~40 to 90 nPa. For these pressures the magnetopause at the subsolar point would be expected to approach very close to the planetary surface if it were not for the effect of the inductions currents. Indeed, Jia et al. found that the induction currents increased the planetary magnetic moment by up to ~25% during these mostly CME-related solar wind events (Jia et al., 2019).

However, as illustrated in Figure 1b, magnetic reconnection at the dayside magnetopause transfers magnetic flux to the nightside magnetosphere and reduces the distance from the center of Mercury to the nose of magnetosphere where the solar wind is “stood off” by the planetary magnetic field. In fact, Slavin and Holzer (1979) scaled Earth observations of the reduction in the radius of the dayside magnetosphere due to reconnection to Mercury. This study, which predated the induction analysis of Hood and Schubert (1979),

predicted that the dayside magnetopause might be frequently be eroded to the surface when the IMF was southward and reconnection rate maximized. Consistent with the predictions of both of these earlier studies, the IMF for seven of the eight highly compressed dayside magnetospheres examined by Jia et al. (2019) occurred during intervals of northward IMF when erosion would be expected to be minimal. Under these conditions the dayside magnetosphere is indeed expected to reach its maximal state of compression before the magnetopause altitude becomes too low to be observed by MESSENGER.

Several previous studies using MESSENGER's magnetic field data have noted passes over the dayside hemisphere for which no low-latitude magnetopause was detected (Raines et al., 2015; Slavin et al., 2019; Zhong, Wan, Slavin, et al., 2015), but no systematic or detail analysis was conducted. The reason for the dayside magnetosphere being absent, or "disappearing," on such occasions could be enhanced solar wind dynamic pressure that compressed the closed magnetic flux down below MESSENGER's orbit or even into the low-conductivity crust overlaying Mercury's highly conducting interior (see Dong et al., 2019 ; Jia et al., 2015). Alternatively, reconnection-driven erosion of the dayside magnetosphere could be responsible (Slavin & Holzer, 1979; Slavin et al., 2009, 2010; Heyner et al., 2016; Jia et al., 2019). However, the high-intensity solar wind and IMF required to compress the dayside magnetic flux down into the low electrically conducting crust (e.g.,Hood & Schubert, 1979 ; Suess & Goldstein, 1979) and/or transfer the magnetic flux into the magnetotail through reconnection (Slavin & Holzer, 1979) would have to be much greater than the CMEs and high-speed stream events observed early in the MESSENGER mission and analyzed by Slavin et al. (2014).

Here we have surveyed all four years of the MESSENGER magnetometer (MAG) (sample rate 20 s; Anderson et al., 2007) and the Fast Imaging Plasma Sensor (FIPS) (complete energy per charge and composition scan of ions up to 13 keV/e in 10 s) (Andrews et al., 2007). Due to the placement of FIPS on the MESSENGER spacecraft, full plasma moments can only be derived under certain sets of assumptions (Raines et al., 2011; Gershman et al., 2012, Gershman et al., 2013; Dewey et al., 2018). Because those assumptions are not typically met in the magnetosheath plasma analyzed here, we present only energy spectra and observed ion densities without correction for any plasma outside the field of view (Raines et al., 2013). Heavy ions are collected into two groups by mass per charge (m/q), i. e. the O^+ (m/q 16–20) and Na^+ groups (m/q 21–30; Raines et al., 2013). All dayside passes over the northern hemisphere for which the low-pass-filtered B_z component of the magnetic field never became positive and FIPS data, if available, showed only H^+ energy spectra typical of the shocked magnetosheath have been identified as disappearing dayside magnetosphere events. Although there are other passes for which FIPS indicates that MESSENGER only entered the magnetosphere intermittantly, here we examine only the four pristine disappearing dayside magnetosphere events identified for which no magnetic fields consistent with the closed dayside magnetosphere were observed in the MAG data. They occurred on 15 October 2011 (or day of year (DOY) 288, 2011), 1 December (DOY 335) 2013, 13 February (DOY 044) 2014, and 25 March (DOY 084) 2015.

An overview of the magnetic field measurements taken by MESSENGER on 15 October 2011 is displayed in Mercury Solar Magnetospheric (MSM) coordinates in Figure 3. In this system the X_{MSM} axis points from the offset location of Mercury's dipole toward the Sun, the Y_{MSM} axis lies in Mercury's equatorial plane and it is positive in the direction opposite to planetary motion, and Z_{MSM} completes the right-handed orthogonal system. The solar wind aberrated frame is indicated by the primes, X'_{MSM}, Y'_{MSM}, and Z'_{MSM}. Aberration is carried out in the same manner as for the MSO system, but with the rotation taking place about the location of the offset magnetic dipole. At this stage of the mission the spacecraft was still in its 12-hr orbit and two periapsis passes (at ~60° north latitude) occurred each Earth day. These periapses are apparent by the large-amplitude maxima in the total magnetic field in Figure 3. On this day MESSENGER moved from lower to higher latitudes over the mid-morning time sector as it approached its periapsis. The IMF intensity at the beginning of the day was only ~10 to 20 nT and the magnetic field was relatively structureless. As indicated in Figure 3 an interplanetary shock (IP SH) arrived at Mercury at ~08:30 UTC and the IMF increased to ~50 nT. About 3 hr later the IMF suddenly increased again to ~90 nT and the level of fluctuations in the magnetic field decreased signaling the arrival of the CME. A broader study of CME signatures in the MESSENGER MAG data at Mercury, including this event, can be found in Winslow et al. (2015).

The highly disturbed nature of Mercury's magnetosphere during the second pass is readily apparent by comparison with the first. The periapses for these two passes occurred at similar altitudes, that is, 330

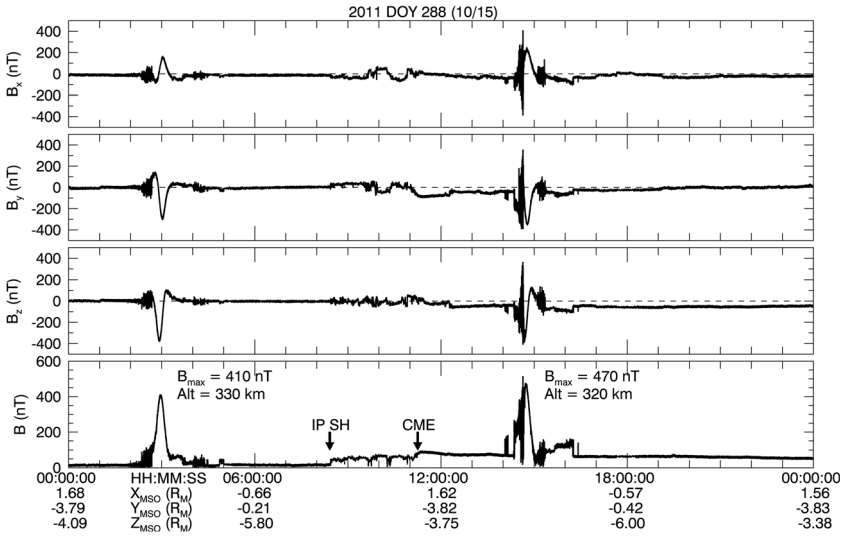

Figure 3. Full resolution (20/s) MAG measurements in MSM coordinates for 15 October 2011. Probable identifications for the arrival of an interplanetary shock and a coronal mass ejection are indicated. The peak magnetic fields for the two periapsis passes are displayed along with the altitudes where they were recorded.

versus 320 km, respectively. Given the mean radius of Mercury, 2,440 km, the change in the total magnetic field due to this small difference in periapsis altitude between the two passes would be only ~1% as compared with the observed increase from the first to the second periapsis of 15%. In addition, the magnetic field variance behind the bow shock is very high for the second pass and the magnetic field intensity drops to very low levels just before large-amplitude magnetic field fluctuations appear. The magnetic field then becomes steady and directed into the northern polar cap where a peak field of ~470 nT was measured. After the outbound bow shock, the IMF is observed to be quite steady, but very intense with a magnitude of ~70 nT.

All four of the DDM events examined here took place during coronal mass ejections that were modeled using the WSA-ENLIL+ Cone algorithm (Odstrcil et al., 2004; Toth & Odstrcil, 1996; Baker et al., 2009, 2013; Dewey et al., 2015). Our focus here is on the magnetospheric measurements made by MESSENGER, not the nature of the CME-drivers. However, we display at the top of Figure 4 for context the solar wind radial velocity, V_r (Figure 4a), and the density, n (Figure 4b), in the ecliptic plane from our WSA-ENLIL simulation for the first DDM event on 15 October 2011. This simulation uses CME input parameters from Community Coordinated Modeling Center's (CCMC) Space Weather Database Of Notifications, Knowledge, and Information (http://ccmc.gsfc.nasa.gov/donki). The predicted time of arrival of the CME at Mercury is ~15:00 UTC or a little over 7 hr after the arrival of the IP SH. The observed arrival time of the IP SH and CME in the MESSENGER data at 08:30 and 11:15 UTC, respectively, are reasonably consistent with the WSA-ENLIL + Cone predictions (e.g., see Dewey et al., 2015). The solar wind density dial depicts the expected compression signatures as the higher-speed solar wind overtakes the slower solar wind. Please note that the plasma density has been multiplied by the square of radial distance (in units of AU) from the center of the Sun to detrend for the decrease in density with increasing distance.

A zoomed-in view of the magnetic field measurements during the second periapsis pass on 15 October 2011, just after the passage of the IP SH and the arrival of the CME, is shown in the bottom panels of Figure 4. The three components and the total magnetic field intensity are shown in Figures 4c–4f. The IMF upstream of the bow shock had an intensity of ~70 nT with $B_z \sim -45$ nT. Around 14:21:22 UTC the spacecraft crossed the bow shock and entered the magnetosheath at an altitude of 1,770 km, a magnetic latitude of 25.4°, and a local time (LT) of 08:10. The average intensity of the magnetic field in the magnetosheath, indicated by the smoothed red trace, was ~200 to 220 nT, $B_z \sim -120$ to -140 nT, and the level of fluctuations was significantly elevated over the earlier solar wind interval. The smoothed magnetic field data shown with the red traces were created by performing a boxcar averaging on the magnetic field data using a 40-s window.

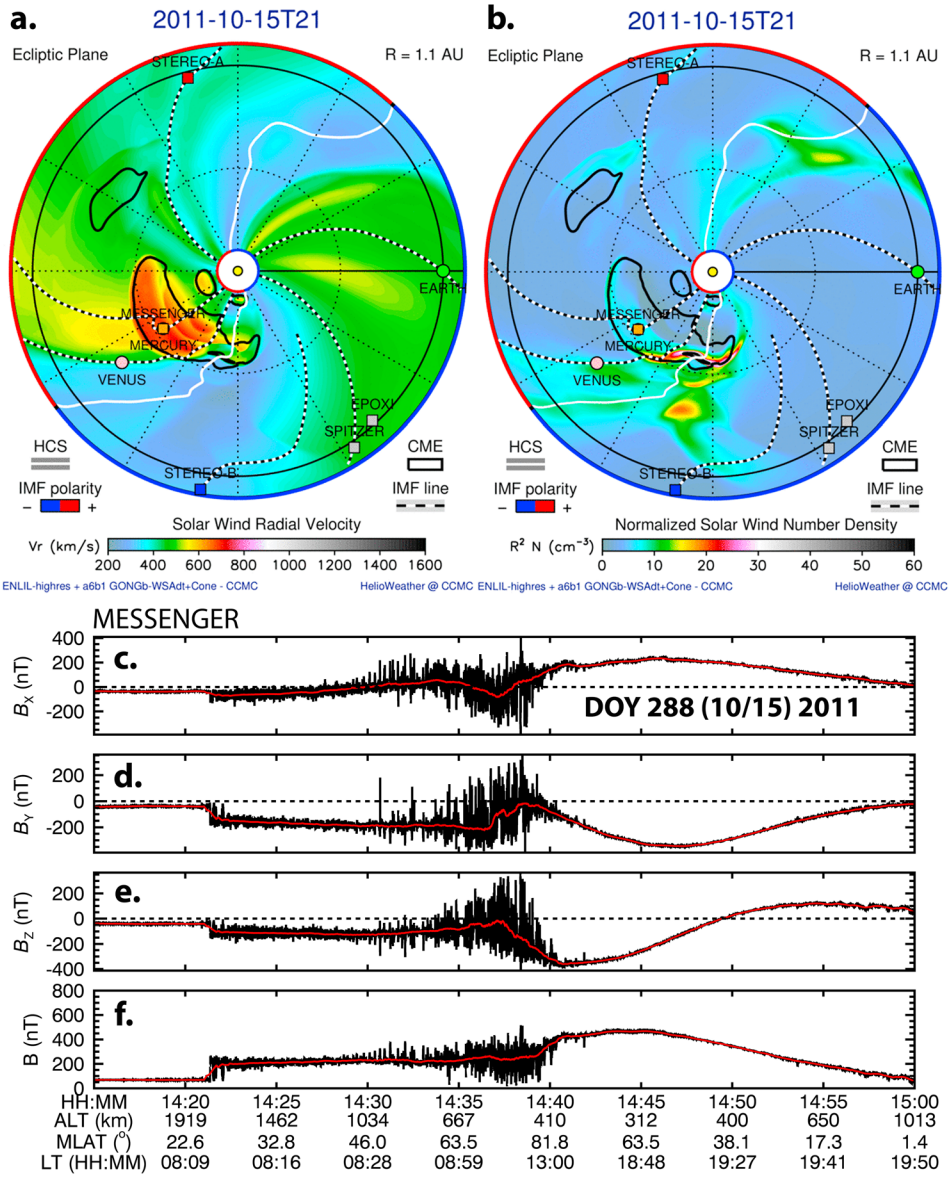

Figure 4. ENLIL-WSA + Cone models of (a) solar wind radial speed (V_r) and (b) the product of solar wind density (n) and the square of distance (r) from the Sun in AU for 15 October 2011 at 21:00 UTC. Coronal mass ejections identified in the SOHO and STEREO observations are enclosed by solid black lines. The center of a coronal mass ejection impacted Mercury and its magnetosphere (yellow circle). The locations of Earth, Venus, and Mercury are all indicated by small colored dots. The inner domain of the model (where WSA is utilized) is denoted by the central white circle. (c and d) Magnetic field B_z and total intensity (B) measurements (sampled at a rate of 20 s). The smoothed magnetic field data are shown with the red traces.

Further, the fluctuations grow in amplitude as MESSENGER moved toward lower altitudes and periapsis. What is most interesting about these magnetic field measurements for the purpose of this study is that the mean B_z component of the magnetic field did not become northward anywhere over the dayside hemisphere of Mercury during this pass. The appearance of northward magnetic fields as soon as the dayside magnetopause is crossed is the most fundamental and clearest signature of the dayside magnetosphere at Mercury (and Earth). However, in Figure 4 the usual inbound magnetopause crossing at an altitude of ~1,000 to 1,500 km is not present. Rather, the magnetopause is not encountered until MESSENGER was at 80° northern magnetic latitude just sunward of the terminator. Following this magnetopause crossing the magnetic field became much steadier and stronger as the high-latitude magnetotail was entered.

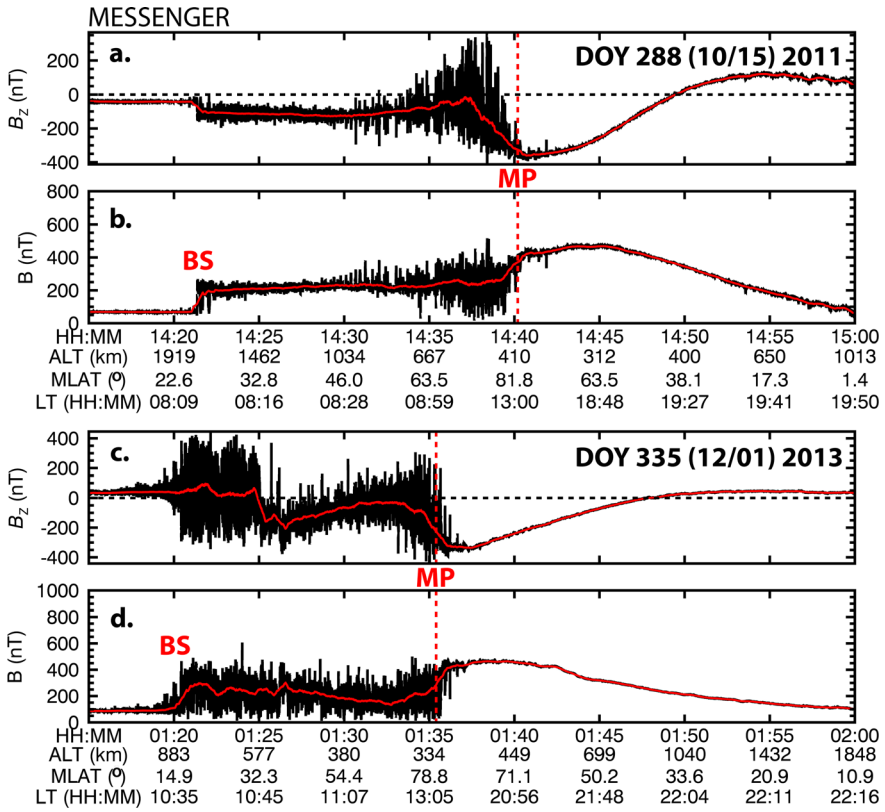

Figure 5. MESSENGER measurements of B_z and B magnitude (20/s) in in MSM coordinates on 15 October 2011and 1 December 2013. The interval presented covers the upstream interplanetary medium, the dayside pass from the low-latitude bow shock (BS) to the high-latitude magnetopause (MP) crossings, and finally the near-tail. Large-amplitude, high-frequency fluctuations are observed from the bow shock through to the magnetopause where they quickly decrease in amplitude.

In Figure 5 the full resolution and smoothed magnetic field B_z and B-total traces for the dayside passes during the 15 October 2011 and 01 December 2013 DDM events are compared and contrasted. The solar wind conditions for the 2013 event were similar to those already described for the 2011 event; an IP SH was followed by a CME impact producing intense and very disturbed planetary magnetic fields consistent with the ENLIL simulation (see Figure 4). In the bottom panels of Figure 5 the similarity between these two dayside passes is quite evident. The upstream IMF in both events is strong, ~50 to 100 nT, due to the arrival of the CME. However, for the 2013 pass the B_z component upstream is slightly positive, but it then turns strongly southward about 5 min after the bow shock is crossed to produce a magnetosheath field of $B_z \sim -200$ nT. As shown, the smoothed magnetic field was southward throughout the rest of the dayside pass until the magnetopause is crossed at very high latitudes, that is, at 80° north magnetic latitude. Again, very large amplitude fluctuations are observed in the magnetic field until the magnetopause is crossed. At this point the magnetic field intensifies as the magnetic field becomes steadily southward over the northern polar cap.

The other two DDM events were recorded by MESSENGER on 13 February 2014 and 25 March 2015 and the MAG measurements are displayed in Figure 6. Both passes were preceded by IP SH's and likely CMEs, based upon the magnetic field observations and ENLIL-WSA + Cone simulations (not shown). The only differences between the events in Figures 5 and 6 are (1) the somewhat more intense upstream IMF intensities for the 2014 and 2015 events that approached 150 nT; (2) the stronger southward B_z in the magnetosheath, ~ −300 to −400 nT; and (3) these magnetopause crossings occurred at somewhat lower magnetic latitudes of 66° and 76°, respectively. Note that these lower latitude magnetopause encounters, presumably due to the more intense negative upstream B_z, also occurred at lower altitudes, ~276 and 254 km, respectively.

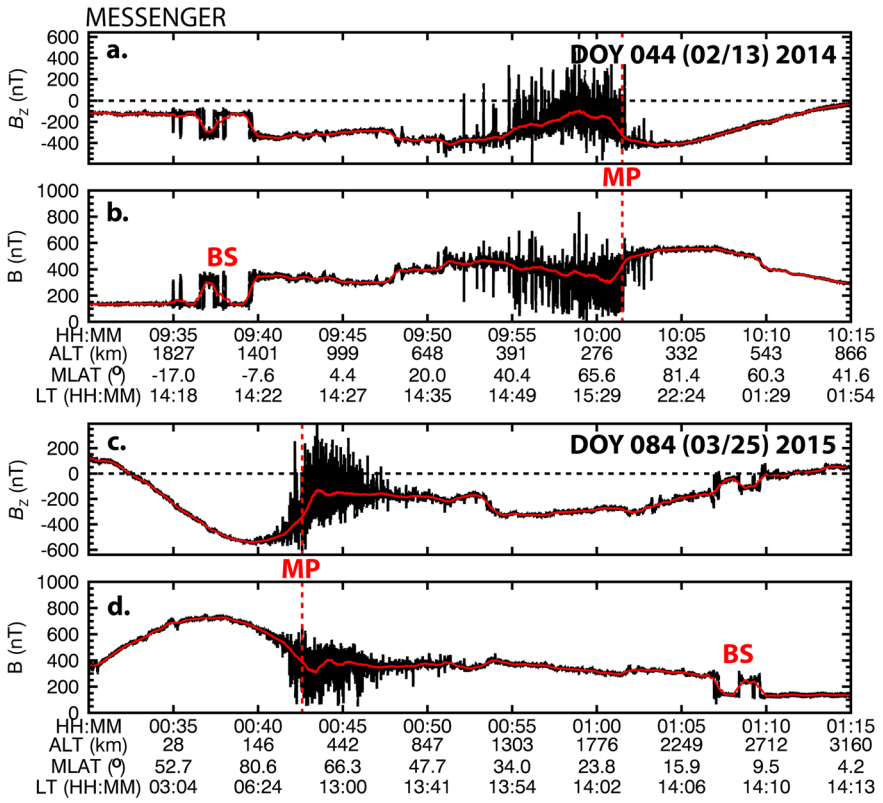

Figure 6. MESSENGER measurements of B_z and B magnitude (20/s) in in MSO coordinates on 13 February 2014 and 25 March 2015. The interval presented covers the upstream interplanetary medium, the dayside pass from the low-latitude bow shock (BS) to the high-latitude magnetopause (MP) crossings, and finally the near-tail. Note that the final DDM event in the bottom panels is the only descending pass wherein MESSENGER passed from the high-latitude tail, through the magnetopause and then ended the dayside pass by exiting through the bow shock at low latitudes. As with the other DDM evens large-amplitude, high-frequency fluctuations are observed throughout these dayside passes.

4. DDM Magnetosheath Plasma Observations

The FIPS plasma measurements for the first three of the DDM dayside passes are displayed in Figure 7. No FIPS measurements are available for the final 25 March 2015 pass due to noise generated within the instrument by penetrating solar energetic particle radiation that accompanied the CME that produced this DDM event. The top panels show the FIPS H^+ energy spectra over a 20-min interval behind the bow shock on 15 October 2011 while MESSENGER was moving northward over the midmorning dayside hemisphere (see the trajectory trace labeled 288 in Figure 8). Under more typical conditions the spacecraft would have crossed the magnetopause in the ~1,200–1,500-km altitude region. However, the H^+ E/q spectra in the top panel and the H^+ density in the second panel show that MESSENGER remained in the magnetosheath observing very hot protons with a mean energy of ~ 1 keV until the magnetopause was crossed at 14:40 UTC. At this point the spacecraft entered the high-latitude magnetosphere at an altitude of 410 km and a local time of 13:00. At ~14:35 UTC the H^+ density and temperature, and the He^{++} density in the third panel, increase just as the amplitude and the frequency of the short-duration spikes in B-total increase in Figure 7d. It is expected that the He^{++} density tracks with that of the H^+ since they are both of solar wind origin. While He^+ is thought to also originate from Mercury (Raines et al., 2013), those ions have only a very low probability of being doubly ionized so that He^{++} originating from the planet is expected to be negligible. After 14:35 UTC the amplitude and frequency of occurrence of these discrete magnetic structures increase as the mean magnetic field intensity increased from ~200 to ~250 nT and B_z decreased from ~ −100 to ~ −250 nT. Again, for a typical pass this is the region where the spacecraft would be expected to transition from the closed dayside magnetosphere into the northern cusp (e.g., Poh et al., 2016 ; Raines et al., 2014 ; Winslow et al., 2012). Further, it is in this region that Na^+-group ions are first observed during this dayside pass as displayed in the

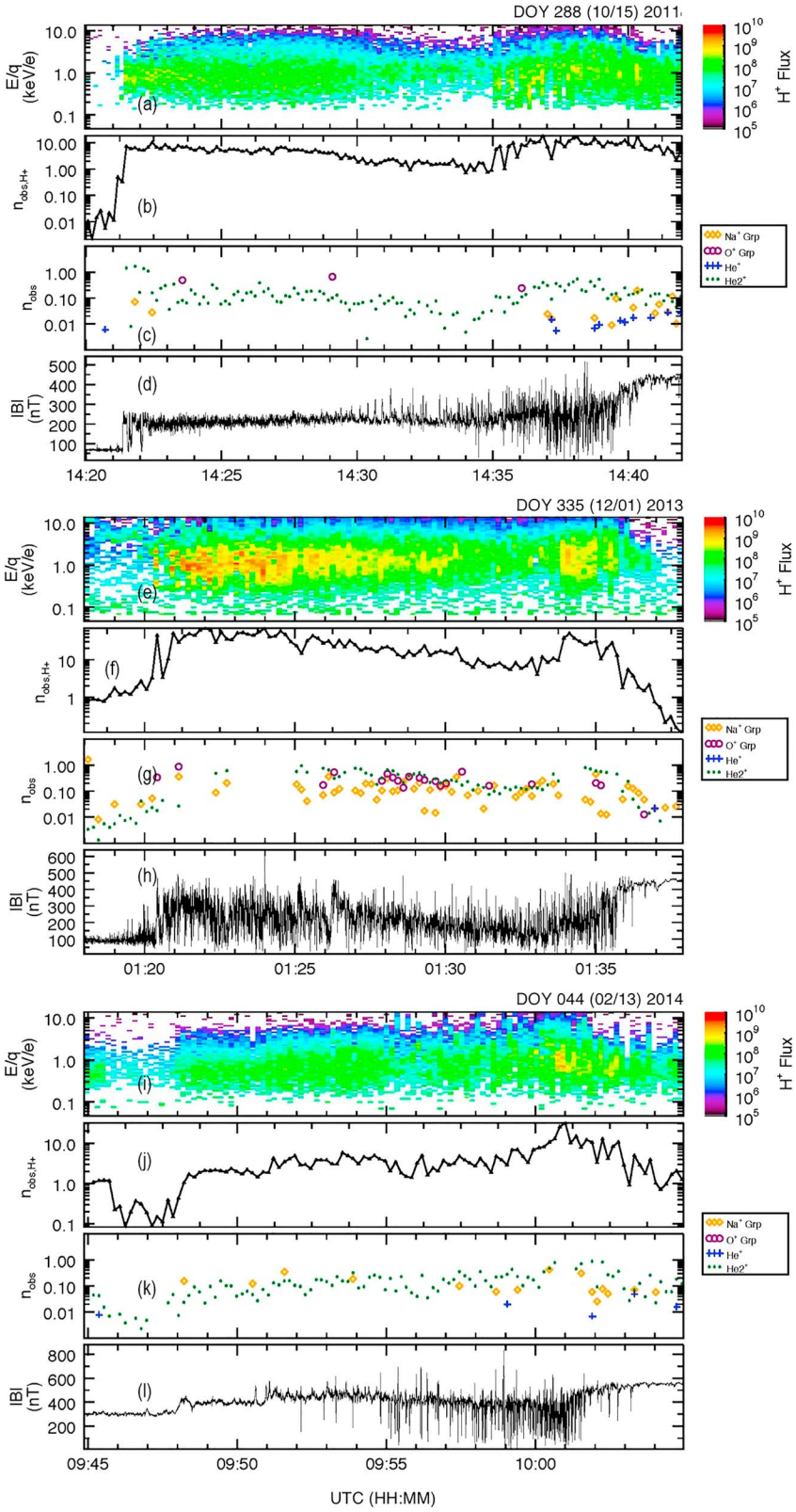

Figure 7. Close-up views of the FIPS plasma measurements for each of the three DDM dayside passes. The FIPS H^+ E/Q spectra ($cm^{-2}\ s^{-1}\ sr^{-1}\ keV^{-1}$); H^+ observed density (cm^{-3}); He^+, He^{++}, O^+, and Na^+ observed densities (cm^{-3}); and *B*-total (nT) are shown in (a)–(d) for the 15 October 2011 events, in (e)–(h) for 1 December 2013, and in (i)–(l) for 13 February 2014.

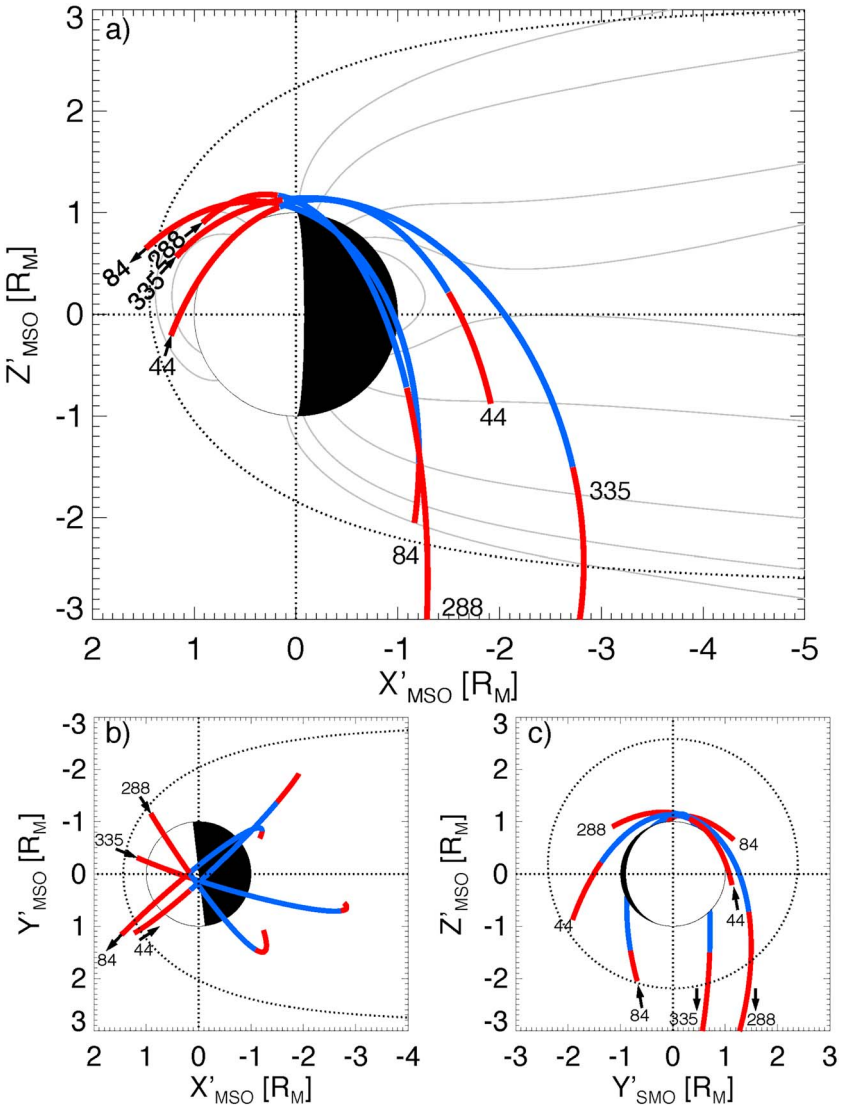

Figure 8. Projections of MESSENGER's trajectory into the aberrated MSO (a) Z'-X', (b) Y'-X', and (c) Z'-X' planes. The background magnetospheric magnetic field lines are from an MHD simulation (Jia et al., 2015). The intervals over which the spacecraft was in the magnetosheath are shown in red while the magnetospheric traversals are shown in blue. Note that arrows indicate the direction of MESSENGER's motion.

Figure 7c. This is where the cusp would usually be located and the observed 0.1–0.2-cm^3 densities are typical of those observed in the cusp. The H^+ density and temperature begin to decrease after the spacecraft passes through the magnetopause near 81°N magnetic latitude very near where the high-latitude "back-wall" of the cusp is usually located. After MESSENGER enters the high-latitude nightside magnetosphere the Na^+ density decreases and the suggestion of an energy dispersion is present in Figure 7a with the higher-energy H^+ becoming depleted as the spacecraft moves to lower latitudes deeper in the northern tail lobe. These observations are all consistent with MESSENGER entering the plasma mantle that makes up the outer high-latitude layer of the magnetotail (DiBraccio et al., 2015; Jasinski et al., 2017).

The FIPS measurements for the 01 December 2013 DDM pass are shown in Figures 7e–7h. Overall, the plasma measurements are remarkably similar to the 2011 event. Again, the magnetosheath interval ends at very high latitudes with the H^+ density and temperature increasing again just before passing through the magnetopause and entering the high-latitude nightside magnetosphere. Na^+-group and other heavy planetary ions are observed throughout the magnetosheath pass. The observed densities of Na^+-group ions are typical of those passes, although the O^+-group ion density is higher than typically observed (Raines et al.,

2014). Finally, plasma mantle density decreases and energy dispersion is observed again as MESSENGER passes more deeply into the northern lobe of the magnetotail. The plasma measurements for the 13 February 2014 DDM magnetosheath pass are displayed in Figures 7i–7l. Again, they are remarkably similar to the two earlier DDM passes in almost every aspect (see the trajectory trace labeled 044 in Figure 8).

The trajectories of MESSENGER for each of the four DDM event passes are plotted in Figure 8. The portion of each of the four DDM periapsis passes with MESSENGER outside of Mercury's magnetosphere are plotted in red while the magnetospheric parts are in blue. The orbits, plus Mercury and its magnetosphere, are then projected into the aberrated MSO Z'-X', Y'-X', and Z'-Y' planes. As shown, the four DDM periapsis passes would certainly have entered the dayside magnetosphere, if it had been present during these MESSENGER periapsis passes. Further, there is general agreement among the 4 passes that the point where the high-latitude nightside magnetosphere was entered just sunward of the north magnetic pole.

5. DDM Flux Transfer Events

When MESSENGER crossed the bow shock and entered the magnetosheath and moved northward over Mercury's dayside on 15 October 2011 (see Figure 8) it not only failed to encounter the usual low-to-middle-latitude magnetopause and closed dayside magnetosphere, but also the steady, compressed draped IMF that makes up the plasma depletion layer (Gershman et al., 2013). Inspection of the high-resolution measurements of B-total for this DDM pass in Figure 9b reveals that large-amplitude compressive fluctuations began to increase in frequency of occurrence and amplitude at ~14:30 UTC as the mean magnetic field intensity increased. These fluctuations grew in amplitude as MESSENGER approached cusp latitudes similar to those seen in the other three DDM passes in Figures 9d, 9f, and 9h. However, what stands out most are the brief, several-second-long increases in magnetic field intensity that coincide with large-amplitude $\pm B_z$. These large-amplitude, several second-long structures are flux transfer event (FTE)-type magnetic flux ropes (Imber et al., 2014; Slavin et al., 2012).

The reconnection process involves the formation of multiple X lines which fragment the current sheet into flux ropes (Lee and Fu, 1985). These very small, initially sub-ion-scale flux ropes then appear to grow rapidly due to both continuous reconnection at the X lines and the coalescence of adjacent flux ropes into larger flux ropes (e.g., see Akhavan-Tafti et al., 2018). FTEs have a helical topology that winds magnetic flux about an axial magnetic field near the center of the structure. The axial “core” field in these FTE-type flux ropes is compressed by the tension in those outer layers (Fear et al., 2007; Hasegawa et al., 2010; Raeder, 2006; Rijnbeek et al., 1984; Russell & Elphic, 1978; Trenchi et al., 2011; Zong et al., 2005). For this reason, the magnetic field intensity maximizes at the center of the structure unless strong gradients in the plasma pressure are present. Indeed, Gershman et al. (2016) used observations of solar energetic electrons detected by FIPS while inside of Mercury's magnetosphere to confirm that FTE magnetic fields are connected to the IMF. After formation, the FTEs are then carried tailward by flow in the magnetosheath and pivot about the end of the magnetic fields that map to one of the magnetospheric cusps as the other is transported into the magnetotail (see Cooling et al., 2001). Because the magnetic flux in these FTE-type flux ropes connects to the solar wind at high altitudes and connects to Mercury in the vicinity of either the north or south cusp, the axial magnetic flux carried by these FTEs does contribute to transfer to the magnetic flux transferred from the dayside to nightside magnetosphere in terrestrial style magnetospheres. At Earth the Dungey cycle is dominated by the transfer of magnetic flux that has undergone reconnection only once at a single magnetopause X line with the FTE contribution being very small. However, at Mercury the fraction of the magnetic flux transfer driving its Dungey cycle carried by FTEs appears large, i. e., ~ 30% to 50% of the total (Imber et al., 2014; Slavin et al., 2012).

For each of the four DDM passes the magnetic field has been examined for the presence of FTEs. They were detected based on their bipolar signature in the maximum variance component of the local magnetic field (B_{max}) coinciding with a peak in both the intermediate variance component of magnetic field (B_{int}) and $|B|$. Furthermore, we have used the Lundquist-Burlaga constant-α force-free model to test that the candidate FTEs had a flux rope magnetic topology. Specifically, fitting of this cylindrical force-free flux rope model to a candidate FTE with a chi-square error that is less than a specified maximum is taken to indicate a successful FTE identification. Further, the fitting method determines the impact parameter (i.e., closest approach

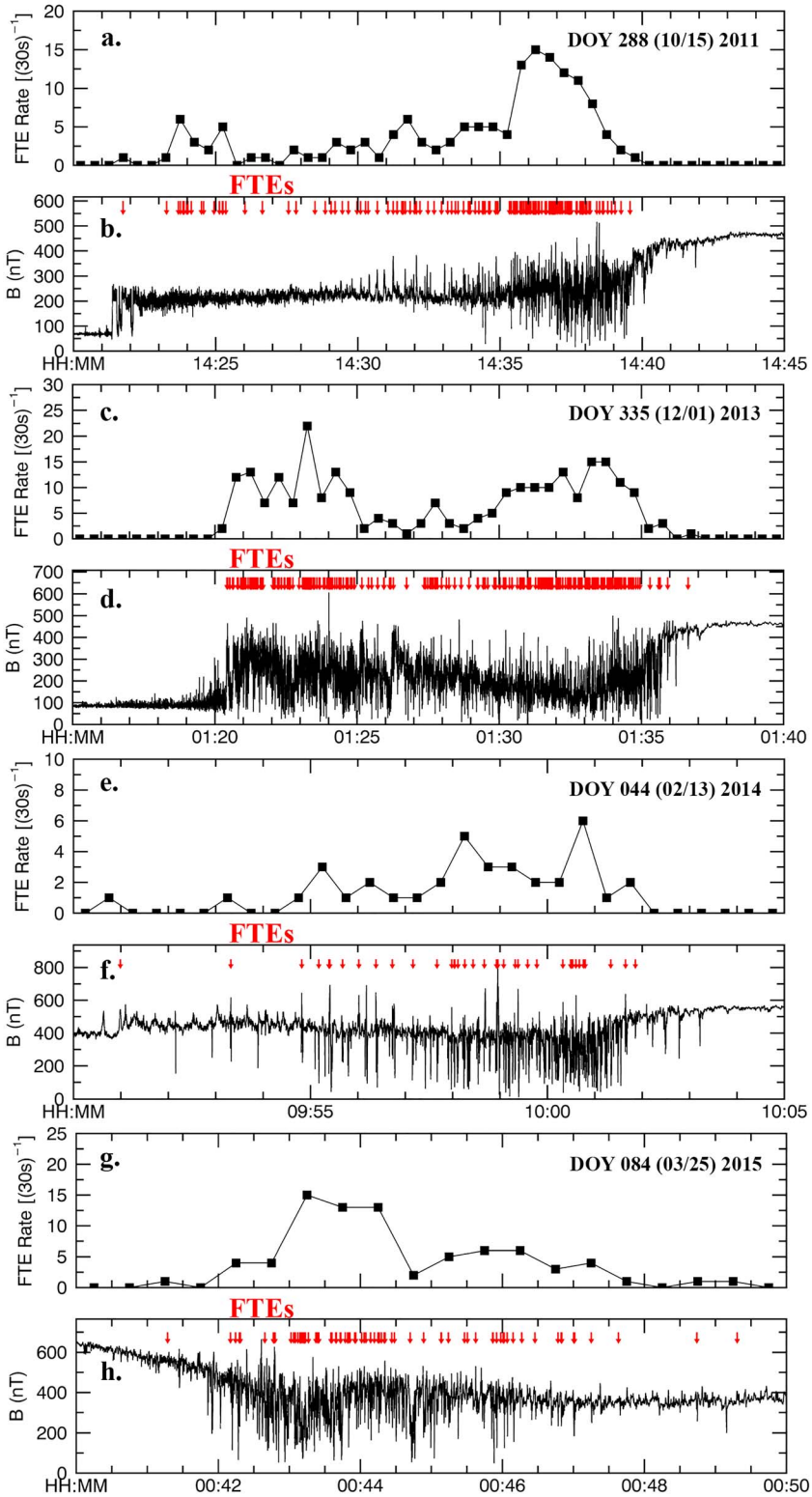

Figure 9. (a, c, e, and g) The rates at which FTEs are observed for each of the DDM passes are displayed in bins of 30-s duration. (b, d, f, and h) For each of the DDM passes red arrows mark the occurrence of individual FTEs against a plot of *B*-total.

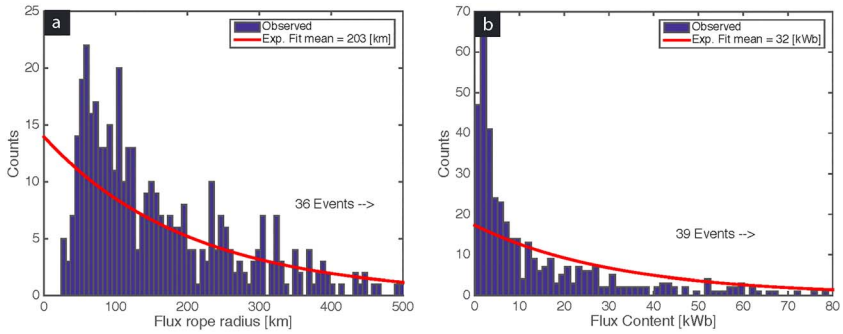

Figure 10. Histograms of (a) FTE radius and (b) FTE flux content for total of 438 FTEs identified and modeled by fitting to a force-free flux rope model (see Akhavan-Tafti et al., 2018).

distance of the spacecraft trajectory to the central axis of the flux rope), the radius of individual FTE-type flux rope and their axial magnetic flux (e.g., Akhavan-Tafti et al., 2018; DiBraccio et al., 2015; Slavin et al., 2003). With the assumption that the thermal pressure gradient is negligible across the structure, force-free FTEs are modeled as a cylinder which contains magnetic flux that is proportional to its size and core magnetic field strength. In addition, the use of the force-free model enables a nonbiased investigation of magnetic structures at the magnetopause. Only structures that satisfy the following criteria are included in the FTE statistics for the DDM events: (i) impact parameter <0.5, (ii) chi-square value <0.1 (see Akhavan-Tafti et al., 2018), and (iii) FTE radius <2,500 km.

For each of the four DDM passes in Figure 9 there are two panels: one that graphs the magnetic field intensity from before the bow shock to a little after the magnetopause crossing to the nightside high-latitude magnetosphere and a second that plots the number of FTEs identified per 30 s accumulation interval. The trajectories for the DDM passes in Figure 8 show that MESSENGER's orbit is providing latitude scans of the frequency of occurrence for the FTEs. Indeed, for these DDM intervals MESSENGER remained in the magnetosheath from near-equatorial latitudes up to ~80°. The frequency of occurrence panels in Figure 9 show that the number of FTEs increase from a few per 30-s bin in the high-altitude magnetosheath just inside the bow shock at low latitudes to a highly reproducible peak of ~15 per 30 s, or 30 FTEs/min, at cusp latitudes. A maximum near the cusp is expected because one end of each of these FTE-type flux ropes must map to the north magnetic pole and pivot about the cusp as they are carried tailward by the flow of shocked solar wind in the magnetosheath. The highest rate of FTE occurrence is indeed at cusp latitudes during these DDM passes.

The physical properties of the 438 FTE-type flux ropes identified in the DDM passes are displayed as histograms in Figure 10 and have been fit with exponentials. The mean radius for these FTEs is 203 km, which is ~10 times the estimated solar wind ~1-keV H^+ gyroradius just inside high-pressure magnetopause crossings (Jia et al., 2019; Slavin et al., 2014) and their mean magnetic flux content is 32 kWb. These FTEs being swept into the magnetotail at a rate of 0.5 per second implies a mean contribution to Mercury's cross-magnetospheric potential drop is 16 kV. This value is about half of the total potential drops estimated from the Dungey cycle loading-unloading of the tail with magnetic flux (Imber and Slavin, 2017) and the energy dispersion in the plasma mantle ions (DiBraccio et al., 2015; Jasinski et al., 2018). Further, this FTE flux transfer rate is comparable to that estimated for the non-FTE magnetic flux being transferred to the magnetotail (DiBraccio et al., 2013; Imber et al., 2014; Slavin et al., 2009). Alternatively, if we take half of the typical Dungey cycle, ~90 s (Imber and Slavin, 2017), to be the time it takes to cycle all of the FTEs at the dayside magnetopause into the tail, then the total magnetic flux contained in all dayside FTEs at a given moment is ~90 s × 16 kWb/s or ~1.4 MWb. This compares with typical tail lobe magnetic flux contents of ~2.5 to 3 MWb (Johnson et al., 2012; Slavin et al., 2012) and a total planetary magnetic flux closing exterior to Mercury of $2\pi\ M_o/R_M$ or 7–9 MWb depending upon the Mercury magnetic moment value assumed (Slavin et al., 2009, 2010). Hence, we conclude that during DDM events the large number of FTE-type flux ropes, and the associated non-FTE open magnetic flux being transferred to the tail lobes constitutes a rersevoir of magnetic flux comparable to the average open magnetic flux content of the magnetotail.

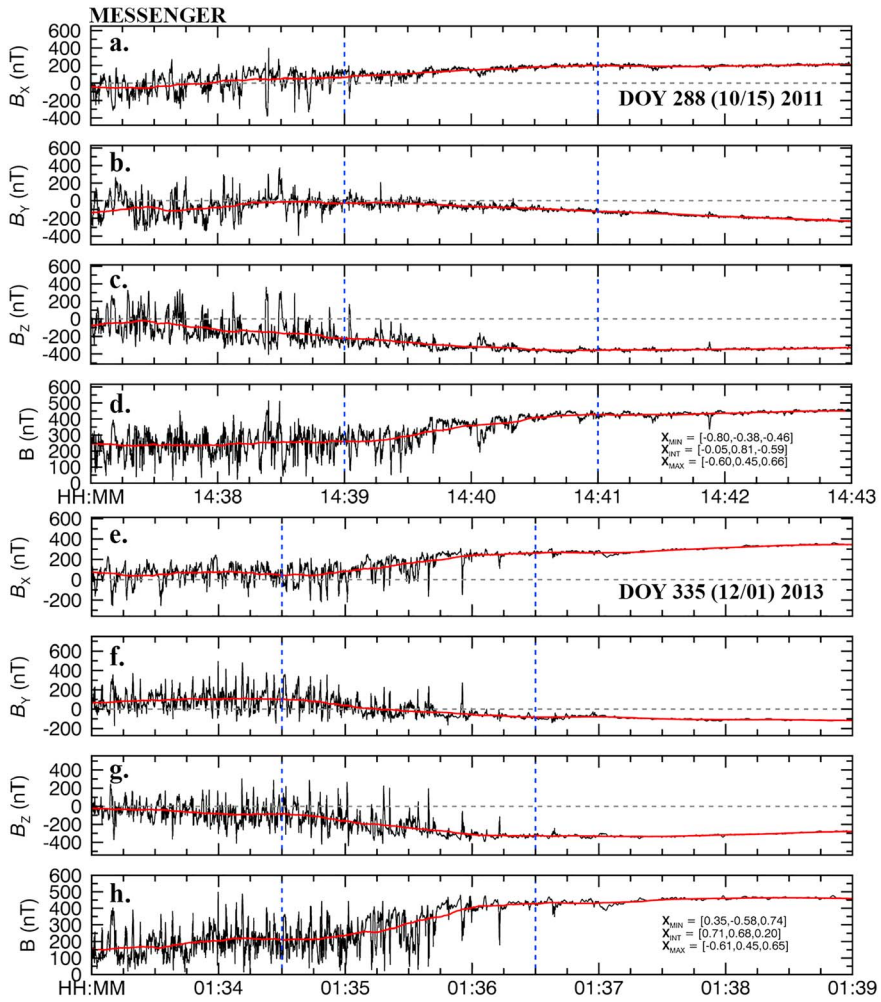

Figure 11. MESSENGER MAG measurements (20 s) in MSM coordinates are displayed across the high-latitude magnetopause crossings for the 15 October 2011 and 01 December 2013 disappearing dayside magnetosphere events. The smoothed magnetic field data shown with the red traces were created by performing a boxcar averaging on the magnetic field data using a 40-s window and used for minimum variance analysis. Vertical dashed lines mark the intervals used for MVA analysis and the minimum, intermediate, and maximum eigenvectors are listed in (d) and (h).

6. DDM Magnetopause Analysis

The MESSENGER magnetic field data for the DDM magnetopause crossings are displayed in more detail in Figures 11 and 12. In each instance the crossing interval is marked by two blue vertical dashed lines. Given the presence of large-amplitude FTEs and cusp plasma filaments (Poh et al., 2016), the red trace graphs the magnetic field smoothing using 40-s boxcar averages. The magnetic field measurements from 14:37 to 14:43 UTC during the first DDM pass on 15 October 2011 are displayed in Figures 11a–11d. The magnetosheath data on the left-hand side have frequent, large-amplitude fluctuations, many of which are flux transfer events that were analyzed and discussed in the previous section. As expected for a CME-impact interval the magnetic field intensities outside and inside of the magnetopause are of similar intensities at ~300 and 400 nT (see Slavin et al., 2014), respectively, presumably due to low upstream Alfvénic Mach numbers (Gershman et al., 2013). A number of magnetopause current sheet crossings are present between ~14:39 and 14:41 UTC and set off with vertical dashed lines.

Minimum variance analysis (MVA) was performed on the 1-s resolution smoothed MAG data shown in Figure 11. The minimum, intermediate, and maximum variance eigenvectors are well defined with intermediate to minimum and maximum and intermediate eigenvalue ratios of 16 and 80, respectively. The eigenvectors in solar wind aberrated MSM coordinates are shown in Figure 11. The ratio of the magnetic

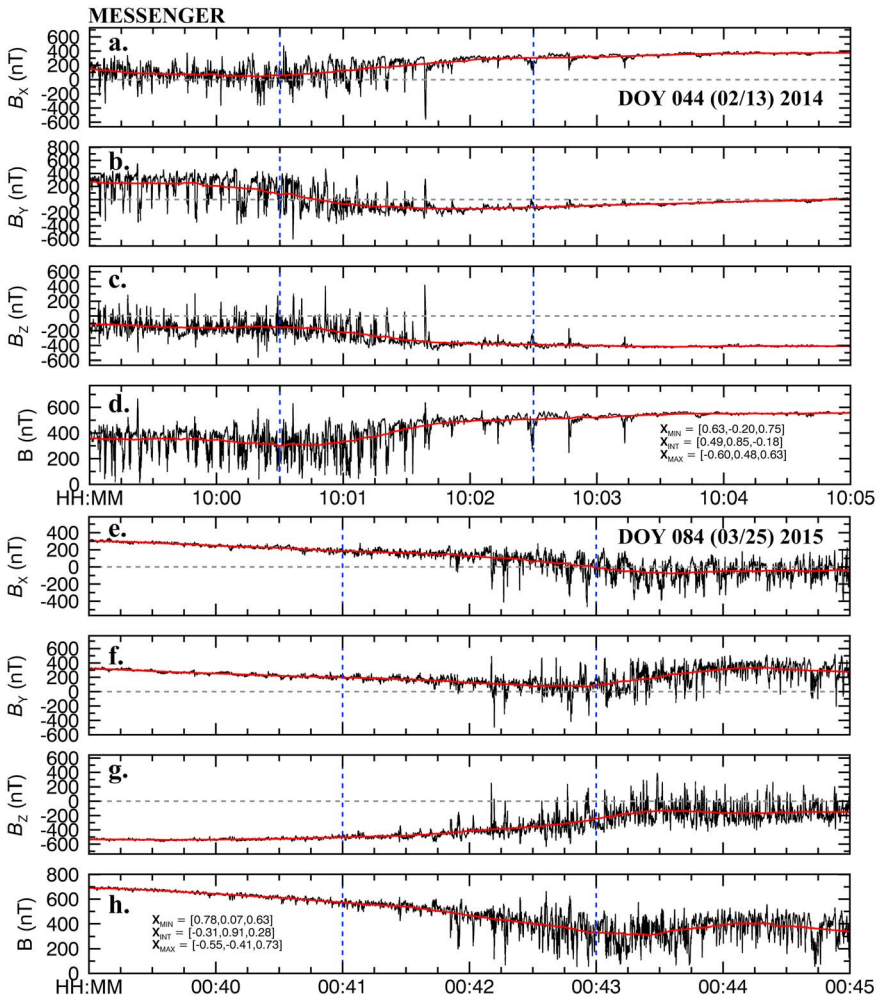

Figure 12. MESSENGER MAG measurements (20/s) in MSM coordinates are displayed across the high-latitude magnetopause crossings for the 13 February 2014 and 25 March 2015 disappearing dayside magnetosphere events. The smoothed magnetic field data shown with the red traces were created by performing a boxcar averaging on the magnetic field data using a 40-s window and used for minimum variance analysis. Vertical dashed lines mark the intervals used for MVA analysis and the minimum, intermediate, and maximum eigenvectors are listed in (d) and (h).

field component normal to the magnetopause to the magnetic field just inside the current layer, which is a measure of the reconnection rate, is 0.12. This value is comparable to the ratios determined for the dayside magnetopause at Mercury in previous studies (Slavin et al., 2008, Slavin et al., 2009; DiBraccio et al., 2013; Liljeblad et al., 2015; Jia et al., 2019; Dong et al., 2019).

The normal component of the magnetic field to the magnetopause, B_N; the dimensionless reconnection rate, α; the dynamic pressure, P_{sw}; and the subsolar standoff distance of the magnetopause, R_{ss}, are summarized for all 4 DDM passes in Table 1. They were determined using the same methods and expressions as used in

Table 1
Magnetopause Analysis Results

Year	DOY	UTC	Type[a]	$X'_{MSM}, Y'_{MSM}, Z'_{MSM}$ (R_M)	$B_N/\|B_N\|$	B_N (nT)	α[b]	P_{sw} (nPa)	R_{ss} (R_M)
2011	288	14:39:00	DDM	(0.13, 0.05, 0.96)	(0.80, 0.38, 0.46)	51.87	0.12	142.4	0.66
2013	335	01:34:30	DDM	(0.13, 0.08, 0.93)	(0.68, 0.01, 0.74)	68.60	0.16	181.9	0.64
2014	44	10:00:30	DDM	(0.09, 0.24, 0.88)	(0.63, −0.20, 0.75)	83.65	0.17	288.5	0.61
2015	84	00:41:45	DDM	(0.17, −0.03, 0.89)	(0.78, 0.08, 0.63)	165.19	0.29	233.0	0.66

[a]Disappearing dayside magnetosphere (DDM). [b]Dimensional reconnection rate $\alpha = B_N/B_{MP}$.

earlier studies of the highly compressed magnetosphere (HCM) events in the MESSENGER data (Jia et al., 2019; Slavin et al., 2014). Upstream solar wind speeds are generally not measured by MESSENGER, but the locations of the magnetopause crossings in MSM have been aberrated assuming typical solar wind speeds of 400 km/s and Mercury azimuthal orbital speeds as a function of distance from the Sun. Average magnetopause position for each of these events is given in Table 1 using this aberrated system (X'_{MSM}, Y'_{MSM}, Z'_{MSM}) in the fifth column from the left.

Figures 11e–11h show the magnetic field measurements of the magnetopause crossing from 01:35 to 01:39 UTC on 01 December 2013. Unlike the magnetopause crossing on 15 October 2011, the magnetic field magnitude difference between the magnetosheath and dayside magnetosphere magnetic field is greater, by ~200 nT, which suggests a higher Alfvénic Mach number than the 2011 event. MVA is also performed on the smoothed magnetic field measurements (red line) of the magnetopause crossing interval delimited by dashed blue lines. The eigenvectors are well defined with intermediate to minimum and maximum and intermediate eigenvalue ratios of ~5 and 303, respectively, and a slightly higher reconnection rate of ~0.16.

The magnetic field observations for the 13 February 2014 and 25 March 2015 magnetopause crossings are displayed in Figure 12. Overall, these events are quite similar despite differences in the CMEs and the altitudes at which the transitions from the magnetosheath to the magnetosphere occurred (e.g., the 25 March 2015 measurements were taken at an altitude of just ~50 km). The magnetic field intensities in the magnetosheath for these two events were ~50 to 70% of the total magnetic field just inside of the magnetosphere. Frequent large-amplitude fluctuations are evident in the magnetosheath, but short duration, deep decreases in the magnetic field intensity, which Slavin et al. (2014) and Poh et al. (2016) termed cusp filaments are present immediately after MESSENGER entered the magnetosphere. As with the 2011 and 2013 magnetopause crossings, the eigenvectors are well defined for both the 2014 and 2015 events. In these cases, the intermediate to minimum and maximum and intermediate eigenvalue ratios were ~10 and 23 and ~9 and 69, respectively. Similarly, the ratios of the magnetic field component normal to the magnetopause to the magnetic field just inside the current layer are 0.17 and 0.29 for the 2014 and 2015 events, respectively.

The upstream solar wind pressure, P_{sw}, must be derived from the state of compression of planetary magnetic field (Slavin et al., 2014) because of the FIPS field-of-view limitations imposed by MESSENGER's thermal Sun shade. The WSA-ENLIL + Cone simulation (Odstrcil et al., 2004; Toth & Odstrcil, 1996; Zhao et al., 2002) was used to provide valuable context regarding the presence of high-speed streams and coronal mass ejections, but the uncertainties in the predictions themselves and the typical timing errors surrounding arrival times (e.g., Dewey, 2015) are too large to support the sorts of quantitative studies conducted here. For this reason, we, again, follow the methodology of Slavin et al. (2014) and Jia et al. (2019) and assume a Newtonian pressure balance across the magnetopause, the MVA magnetopause normals, and, based upon the FIPS data, that the plasma pressure in the outer dayside magnetosphere is very small compared to the magnetic pressure (Raines et al., 2015). In this case the solar wind pressure computed from the pressure balance condition becomes (Spreiter et al., 1966)

$$P_{sw} = \left(B^2/2\mu_o\right)/\left(0.88\cos^2\vartheta\right) \quad (1)$$

where ϑ in the angle between the magnetopause unit normal and the upstream solar wind velocity vector, which is assumed to be radially outward from the Sun, and 0.88 is effectively a drag coefficient determined from gas dynamic modeling for blunt obstacles (Spreiter et al., 1966). Methods similar to these have been used previously for Earth (e.g., Holzer & Slavin, 1978) and other planets (Crider et al., 2003; Slavin et al., 1985; Slavin & Holzer, 1979). The upstream solar wind pressures inferred for the DDM passes in this manner as listed in Table 1 were 142, 182, 289, and 233 nPa for the 2011, 2013, 2014, and 2015 events. Similarly, the dimensionless reconnection rates, B_N/B_{MP}, for these events were 0.12, 0.16, 0.17, and 0.29, respectively. The mean is 0.19, which is somewhat greater than the mean of rate of 0.13 determined from a larger ensemble of magnetopause crossings by DiBraccio et al. (2013).

7. Discussion

The mean bow shock and magnetopause nose distances determined from the complete set of MESSENGER boundary crossings are ~1.9 and 1.45 R_M, respectively (Winslow et al., 2013). In Figure 13 the bow shock and

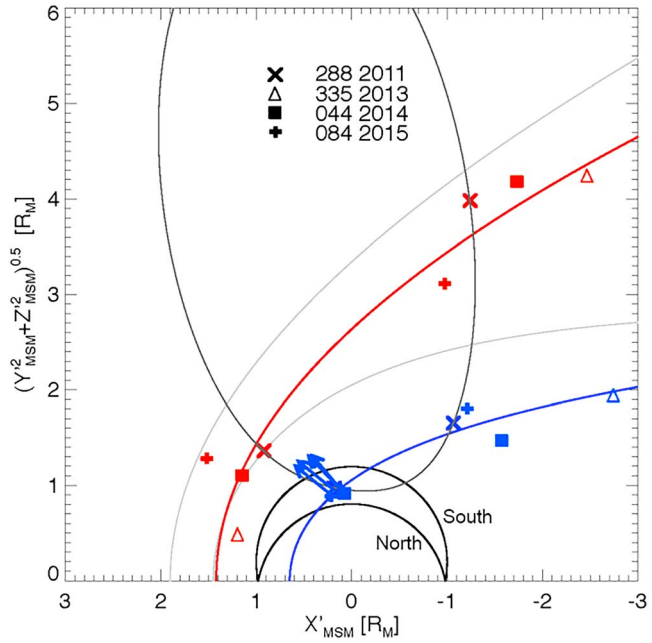

Figure 13. The locations of the bow shock (red marks) and magnetopause (blue marks) observed during the DDM passes are plotted in cylindrical solar wind aberrated MSM coordinates. Shue et al. (1997) boundary surfaces have been fit to the bow shock and magnetopause crossings and displayed in red and blue, respectively. For comparison the surface of Mercury and the much higher altitude mean surface determined by Winslow et al. (2013) are also displayed in gray.

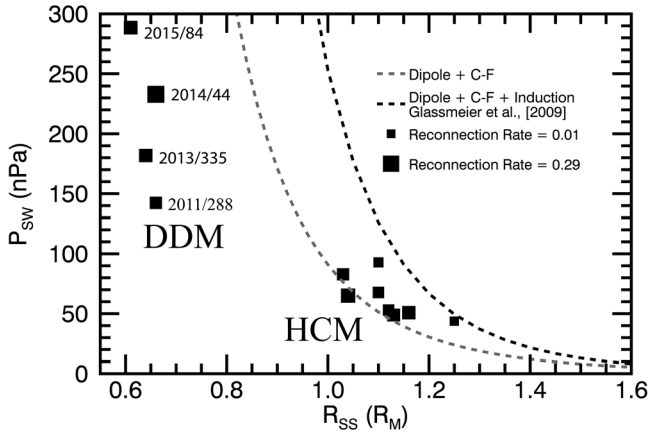

Figure 14. The extrapolated standoff distance of the nose of the magnetopause, R_{ss}, is plotted against the upstream solar wind dynamic pressure, P_{sw}, for each of the eight highly compressed dayside magnetosphere (HCM) and four disappearing dayside magnetosphere (DDM) intervals. The individual magnetopause crossings are displayed as square symbols with the size of box proportional to the dimensionless reconnection rate. A Chapman-Ferraro (CF) sixth root of P_{sw} curve intersecting the mean 10–15-nPa standoff distance determined by Winslow et al. (2013) is the lower dashed line. The upper dashed line (black) is a theoretical model of the compression of Mercury's dayside magnetosphere by Glassmeier et al. (2007) that includes the effects of induction in Mercury's interior.

magnetopause crossings observed during the 4 DDM events have been plotted in solar wind aberrated cylindrical MSM coordinates. The best fits obtained by Winslow et al. (2013) to the complete MESSENGER bow shock data set and our fits to the eight DDM shock crossings are shown in gray and red, respectively. For both data sets the Mercury bow shock crossings have been fit using the offset conic surface method of Slavin and Holzer (1981). The shock surfaces for the total MESSENGER data set and the DDM events do not differ greatly in shape, but the nose, or standoff distance, for the DDM bow shock is much closer at 1,196 km, or ~0.5 R_M. Global magnetohydrodynamic or hybrid modeling of the DDM intervals is planned as part of a future study, but the large planetward shift of the bow shock location during these DDM intervals strongly suggests that the solar wind streamlines in the subsolar region intersect the surface. If this is correct, then solar wind impact will take place over some or much of the dayside surface during these DDM events, especially given the low Alfvénic Mach numbers expected during CME impacts (see Slavin et al., 1980; Slavin & Holzer, 1981).

The eight DDM magnetopause crossings have been fit to the Shue model surface (Shue et al., 1997):

$$r = R_{ss}\,[2/(1+\cos\theta)]^b \quad (2)$$

where θ is the solar zenith angle from the subsolar point, b is the magnetopause shape parameter, and R_{ss} the solar wind standoff distance from the center of the obstacle. The mean DDM bow shock surface model for all of the MESSENGER magnetopause crossings was determined to be $b = 0.5$ and $R_{ss} = 1.4\ R_M$ (Winslow et al., 2013). Our best fit of the DDM magnetopause crossings to the Shue surface is shown in solid blue in Figure 13. This surface is quite different from the mean determined for all conditions (see gray solid line in Figure 13) with $b = 0.7$ and $R_{ss} = 0.65\ R_M$. Not only is the DDM magnetopause more flared but it passes below the surface of Mercury forward of the terminator plane in the northern hemisphere and just tailward in the southern hemisphere. Note also in Figure 13 that the magnetopause normals determined using MVA analysis (see Figures 11 and 12) are also displayed as arrows the point where the crossings occurred. As shown these MVA magnetopause normal vectors are very close to expectations based upon the DDM magnetopause model surface.

Our analyses of the four disappearing dayside magnetosphere events identified in the MESSENGER four-year data set are summarized in Figure 14. The solar wind dynamic pressure is shown on the vertical axis and the distance to the nose of the magnetopause, R_{ss}, is on the horizontal axis. In addition to the DDM events, the eight highly compressed magnetosphere events from Jia et al. (2019) are displayed for comparison. Here the P_{sw} and R_{ss} values for all 12 events are plotted in same manner as in Slavin et al. (2014) and Jia et al. (2019).

We note, first, that the HCM event solar wind pressures and R_{ss} values range from ~44 to ~93 nPa and 1.25 to 1.03 R_M, respectively (Jia et al., 2019). In contrast, the solar wind pressures for the DDM events are much larger at ~142 to ~289 nPa (see Table 1). The Chapman-Ferraro sixth root of P_{sw} relationship (Chapman & Ferraro, 1932) with solar wind standoff distance for an ~200 nT-R_M^3 magnetic moment is displayed as a thin dashed gray line. Note that this relationship should hold not only in the

absence of reconnection at the magnetopause or induction inside of Mercury but also if these effects counterbalance each other (Slavin et al., 2014). The P_{sw}-R_{ss} relationship derived by Glassmeier et al. (2007), which includes the effects of induction but not reconnection in Mercury's interior, is shown as a bold dashed line to the right of the Chapman-Ferraro curve. The Chapman-Ferraro model predicts that the nose of the magnetopause should be compressed down to Mercury's surface for a solar wind dynamic pressure of ~90 nPa. This pressure increases to ~200 to 250 nPa when the effects of induction currents on the surface of Mercury's iron core at taken into account (Glassmeier et al., 2007; Hood & Schubert, 1979). By comparison, the typical solar wind standoff distance for the nose of Mercury's magnetopause is only ~1.4 to 1.5 R_M from the center of the planet for an average solar wind pressure of ~10–15 nPa (Winslow et al., 2013).

The size of the boxes in Figure 14 represent the individual magnetopause crossings and they are proportional to the dimensionless reconnection rate, $\alpha = B_N/B_{MP}$, determined for each magnetopause crossing from the MVA analysis as described in DiBraccio et al. (2013). As shown, the dimensionless reconnection rates ranged from 0.01 to 0.29 with the lower rates corresponding mostly to the HCM events and the highest rates to the DDM events. This result is likely due to reconnection at the DDM magnetopause crossings being more symmetric, that is, the ratio of the magnetosheath to the magnetospheric magnetic field intensity being closer to unity during the larger, more impactful CMEs. For a given magnetic shear angle across the magnetopause reconnection rate is expected to be higher for symmetric as compared to asymmetric current sheets (see DiBracio et al., 2013).

The magnetopause crossings in Figure 14 with the highest reconnection rates, i. e., the larger boxes, are associated with the DDM events and these events are located to the left of the Chapman-Ferraro curve. These events have extrapolated subsolar points below the surface, that is, $R_{ss} < 1$ (see Figure 13). In contrast, the HCM events with the highest magnetopause reconnection rates are located closer to the Chapman-Ferraro curve and the crossings with the smallest dimensionless reconnection rates are located closest to the Glassmeier et al. curve on the right-hand side that includes the effects of induction. Overall, these results suggest that reconnection-driven dayside magnetic flux transfer to the magnetotail and the addition of closed magnetic flux to the dayside magnetosphere due to induction currents are in approximate balance for these highly compressed dayside magnetosphere events (see Heyner et al., 2016). For this reason, the HCM events do not appear to expose the dayside to direct solar wind impact; that is, their R_{ss} values are greater than 1. These conclusions are strongly supported by the global MHD simulations of the solar wind interaction with Mercury's magnetic field and conducting iron core by Jia et al. (2019).

In contrast to the HCM events, the DDM events have R_{ss} values between 0.61 and 0.66 (see Table 1), indicating that most of dayside hemisphere experiences direct solar wind impact. If these events were primarily due to compression of the closed magnetic flux down into the crust, then a clustering near R_{ss}~1 would have been expected in Figure 14 because the solar wind cannot exert pressure below the surface due to its absorption and neutralization upon contact with the regolith. For this situation the bow shock would be expected to be located closer to the planet than would be the case if all of the solar wind were deflected by a magnetopause. The reason is simply that some or many of the solar wind flow streamlines would intersect and terminate in Mercury's surface. In contrast, a more distant bow shock and thicker magnetosheath would allow all of them to be deflected about the magnetopause (e.g., see Spreiter et al., 1966; Slavin et al., 1980).

Although heavy ions were present in each of the three events for which plasma data were available, substantially more Na^+-group ions were observed throughout the magnetosheath passage on DOY 335 2013. Raines et al. (2014) hypothesized that the >500-eV heavy ions typically observed in Mercury's northern cusp are energized from <1-eV photo-ions as part of the reconnection process on the dayside magnetopause. As this event is also the one with the highest FTE rates observed throughout the magnetosheath, it is consistent with that hypothesis. The enhanced heavy ion content on DOY 335 2013 is not likely due to seasonal effects (local time). Those effects showed maximum heavy ions in orbits that passed through the dayside close to local times 0900 and 1500, whereas this event passes through at nearly 1200.

The relative contributions of solar wind compression and reconnection-driven erosion to the disappearance of the dayside magnetosphere at the ~250- to 400-km altitudes of the MESSENGER passes presented here is difficult to determine. The very high solar wind pressures inferred from our analyses of the DDM high-latitude magnetopauses are near those required to compress the closed dayside magnetic fields until it is

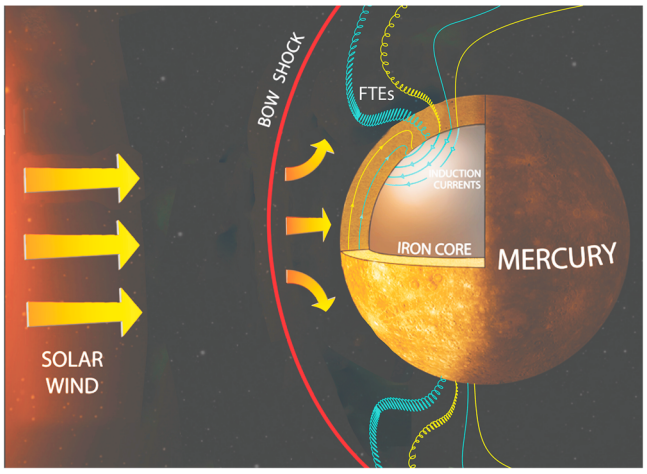

Figure 15. The primary features of the disappearing dayside magnetosphere events are illustrated with the magnetic field lines due to the core dynamo and the induction currents on the core surface, are shown in yellow and green, respectively. The bow shock is very close to the planet presumably due to solar wind impact and absorption. Large numbers of FTE-type flux ropes are observed and an unknown fraction of closed field lines are compressed into the crust by the high solar wind pressure.

trapped between the incident solar wind and the highly electrically conducting iron core (see Figure 1). However, the southward IMF in the dayside magnetosheath is equally impressive with $B_z \sim -100$ to -400 nT and very high rates of FTE-type flux ropes are observed in the magnetosheath as discussed earlier. If the closed field lines on the dayside are eroded by reconnection, that is, opened and transferred to the lobes of the tail, then the high-latitude magnetopause crossings might be expected to move equatorward, enhanced flaring of the tail magnetopause would take place, and the lobe magnetic flux content would be enhanced. As described earlier, there is evidence for each of these effects, but the results are not so clear as those for the extreme solar wind pressure enhancements. Planned studies beyond the scope of the analyses presented here will expand beyond the very pristine disappearing dayside magnetosphere events considered here to include events with a wider range of IMF orientations and intervals for which the dayside magnetosphere is only briefly observed in between intervals of low-altitude magnetosheath.

8. Conclusions

The primary features of the disappearing dayside magnetosphere events are illustrated in Figure 15. The magnetic field lines due to the core dynamo and the induction currents on the core surface are shown in yellow and green, respectively. During the disappearing dayside magnetosphere intervals examined here MESSENGER remained in the magnetosheath for altitudes as low as ~250–300 km below ~80° north latitude. We cannot rule out the existence of some closed dayside magnetic flux below the altitude of MESSENGER, but just above the surface during these DDM events. However, the extremely high solar wind dynamic pressures, more than 2 orders of magnitude above typical levels, the ~ -100 to -400 nT southward magnetic fields in the magnetosheath and the large amount of magnetic flux contained in FTE-type flux ropes at any given moment, i. e., comparable to half of the total open flux in the tail lobes, all argue against a large reservoir of closed magnetic flux at very low altitudes over the dayside hemisphere. Further, as illustrated in Figure 15, the extreme closeness of the bow shock, especially in the subsolar region, suggests continuous direct solar wind impact and absorption on the surface, as opposed to complete diversion about Mercury. Indeed, it is interesting to speculate that terrestrial-type exoplanets orbiting close to low-mass stars, i. e., "hot Earths" (Dong et al., 2017) may often have the shielding capability of their dayside magnetospheres compromised by the same combination of extreme stellar wind ram pressure and magnetic reconnection reported here for Mercury during DDM events.

There are many important questions regarding these DDM intervals that remain to be answered. The relative contributions of magnetic flux created by induction currents flowing on the surface of the planet's iron core, the amount of magnetic flux compressed down into the crust by the high solar wind pressures, and the magnetic flux contained in FTE-type flux ropes and non-FTE magnetic field lines opened by reconnection all need to be understood. Further, the reasons for the very high reconnection rates determined for the DDM high-latitude magnetopause crossings, by a factor of nearly 50% relative to the highly compressed magnetosphere intervals analyzed by Jia et al. (2019), are not known. Indeed, the region(s) where the large numbers of FTE-type flux ropes formed during these DDMs, that is, very low altitude/low latitude closed magnetic fields or at higher latitudes closer to the polar or flank terminator plane, is not understood at all. If direct solar wind impact is as extensive as suggested by Figure 15, then the contribution of solar wind-driven sputtering to Mercury's exosphere should maximize during DDM events. Indeed, future studies of DDM events using global numerical magnetospheric simulations will be necessary before the impact of DDM events on the short- and longer-term solar wind flux reaching Mercury's surface and their role in supporting the neutral exosphere and magnetospheric heavy ion populations through sputtering can be assessed (Killen et al., 2019). The joint ESA–JAXA–NASA BepiColombo mission is scheduled to arrive at Mercury in late 2025. The dual-spacecraft observations to be returned by this mission will provide much new data on the sources of Mercury's exospheric neutrals and magnetospheric ions and the role of direct solar wind impact.

Acknowledgments

We are thankful to the MESSENGER Project and especially the FIPS and MAG instrument teams for providing the plasma and magnetic field data. The FIPS and MAG products used in this paper are available from the Planetary Data System (http://ppi.pds.nasa.gov/). This work was supported by NASA grants NNX16AJ67G, NNX15AL01G, NNX16AJ03G, and 80NSSC18K1137. The WSA- ENLIL + Cone simulation results were provided by the CCMC through their public Runs-on-Request system (http://ccmc.gsfc.nasa.gov; run number Ryan_Dewey_031417_SH_1). The WSA model was developed by N. Arge at NASA GSFC, and the ENLIL model was developed by D. Odstrcil at GMU.

References

Akhavan-Tafti, M., Slavin, J. A., le, G., Eastwood, J. P., Strangeway, R. J., Russell, C. T., et al. (2018). MMS examination of FTEs at the Earth's subsolar magnetopause. *Journal of Geophysical Research: Space Physics*, *123*, 1224–1241. https://doi.org/10.1002/2017JA024681

Alexeev, I. I., Belenkaya, E. S., Slavin, J. A., Korth, H., Anderson, B. J., Baker, D. N., et al. (2010). Mercury's magnetospheric magnetic field after the first two MESSENGER flybys. *Icarus*, *209*(1), 23–39. https://doi.org/10.1016/j.icarus.2010.01.024

Anderson, B. J., Acuña, M. H., Lohr, D. A., Scheifele, J., Raval, A., Korth, H., & Slavin, J. A. (2007). The Magnetometer instrument on MESSENGER. *Space Science Reviews*, *131*(1-4), 417–450. https://doi.org/10.1007/s11214-007-9246-7

Anderson, B. J., Johnson, C. L., Korth, H., Purucker, M. E., Winslow, R. M., Slavin, J. A., et al. (2011). The global magnetic field of Mercury from MESSENGER orbital observations. *Science*, *333*(6051), 1859–1862. https://doi.org/10.1126/science.1211001

Andrews, G. B., Zurbuchen, T. H., Mauk, B. H., Malcom, H., Fisk, L. A., Gloeckler, G., et al. (2007). The Energetic Particle and Plasma Spectrometer instrument on the MESSENGER spacecraft. *Space Science Reviews*, *131*(1-4), 523–556. https://doi.org/10.1007/s11214-007-9272-5

Baker, D. N., Odstrcil, D., Anderson, B. J., Arge, C. N., Benna, M., Gloeckler, G., et al. (2009). Space environment of Mercury at the time of the first MESSENGER flyby: Solar wind and interplanetary magnetic field modeling of upstream conditions. *Journal of Geophysical Research*, *114*, A10101. https://doi.org/10.1029/2009JA014287

Baker, D. N., Poh, G. K., Odstrcil, D., Arge, C. N., Benna, M., Johnson, C. L., et al. (2013). Solar wind forcing at Mercury: WSA-ENLIL model results. *Journal of Geophysical Research: Space Physics*, *118*, 45–57. https://doi.org/10.1029/2012JA018064

Benna, M., Anderson, B. J., Baker, D. N., Boardsen, S. A., Gloeckler, G., Gold, R. E., et al. (2010). Modeling of the magnetosphere of Mercury at the time of the first MESSENGER flyby. *Icarus*, *209*(1), 3–10. https://doi.org/10.1016/j.icarus.2009.11.036

Borovsky, J. E., Nemzek, R. J., & Belian, R. D. (1993). The occurrence rate of magnetospheric-substorm onsets: Random and periodic substorms. *Journal of Geophysical Research*, *98*(A3), 3807–3813. https://doi.org/10.1029/92JA02556

Chapman, S., & Ferraro, V. C. A. (1932). A new theory of magnetic storms, pt. 1, The initial phase. *Terre Magazine*, *37*(2), 147–156. https://doi.org/10.1029/TE037i002p00147

Cooling, B. M. A., Owen, C. J., & Schwartz, S. J. (2001). Role of the magnetosheath flow in determining the motion of open flux tubes. *Journal of Geophysical Research*, *106*(A9), 18,763–18,775. https://doi.org/10.1029/2000JA000455

Crider, D. H., Vignes, D., Krymskii, A. M., Breus, T. K., Ness, N. F., Mitchell, D. L., et al. (2003). A proxy for determining solar wind dynamic pressure at Mars using Mars Global Surveyor data. *Journal of Geophysical Research*, *108*(A12), 1461. https://doi.org/10.1029/2003JA009875

Dewey, R. M., Raines, J. M., Sun, W.,Slavin, J. A., & Poh, G. (2018). MESSENGER observations of fast plasmaflows in Mercury's magnetotail. *Geophysical Research Letters*, *45*, 10,110–10,118. https://doi.org/10.1029/2018GL079056

DiBraccio, G. A., Slavin, J. A., Boardsen, S. A., Anderson, B. J., Korth, H., Zurbuchen, T. H., et al. (2013). MESSENGER observations of magnetopause structure and dynamics at Mercury. *Journal of Geophysical Research: Space Physics*, *118*, 997–1008. https://doi.org/10.1002/jgra.50123

DiBraccio, G. A., Slavin, J. A., Raines, J. M., Gershman, D. J., Tracy, P. J., Boardsen, J. A., et al. (2015). First observations of Mercury's plasma mantle by MESSENGER. *Geophysical Research Letters*, *42*, 9666–9675. https://doi.org/10.1002/2015GL065805

Domingue, D. L., Chapman, C. R., Killen, R. M., Zurbuchen, T. H., Gilbert, J. A., Sarantos, M., et al. (2014). Mercury's weather-beaten surface: Understanding Mercury in the context of lunar and asteroidal space weathering studies. *Space Science Reviews*, *181*, 121–214.

Dong, C. F., Lingam, M., Ma, Y. J., & Cohen, O. (2017). Is Proxima Centauri B habitable? A study of Atmospheric Loss. *The Astrophysical Journal*, *837*, L26.

Dong, C. F., L. Wang, A. Hakim, A. Bhattacharjee, J. A. Slavin, G. A. DiBraccio, K. Germaschewski, A novel ten-moment multifluid model for Mercury: From the planetary conducting core to the dynamic magnetosphere, arXiv:1904.02695 (2019).

Dungey, J. W. (1961). Interplanetary magnetic field and the auroral zones. *Physical Review Letters*, *6*(2), 47–48. https://doi.org/10.1103/PhysRevLett.6.47

Exner, X., Heyner, D., Liuzzo, L., Motschmann, U., Shiota, D., Kusano, K., & Shibayama, T. (2018). Coronal mass ejection hits mercury: A.I. K.E.F. hybrid-code results compared to MESSENGER data. *Planetary and Space Science*, *153*, 89–99. https://doi.org/10.1016/j.pss.2017.12.016

Fear, R. C., Milan, S. E., Fazakerley, A. N., Owen, C. J., Asikainen, T., Taylor, M. G. G. T., et al. (2007). Motion of flux transfer events: A test of the Cooling model. *Annals of Geophysics*, *25*(7), 1669–1690. https://doi.org/10.5194/angeo-25-1669-2007

Gershman, D. J., Dorelli, J. C., DiBraccio, G. A., Raines, J. M., Slavin, J. A., Poh, G., & Zurbuchen, T. H. (2016). Ion-scale structure in Mercury's magnetopause reconnection diffusion region. *Geophysical Research Letters*, *43*, 5935–5942. https://doi.org/10.1002/2016GL069163

Gershman, D. J., Slavin, J. A., Raines, J. M., Zurbuchen, T. H., Anderson, B. J., Korth, H., et al. (2013). Magnetic flux pileup and plasma depletion in Mercury's subsolar magnetosheath. *Journal of Geophysical Research: Space Physics*, *118*, 7181–7199. https://doi.org/10.1002/2013JA019244

Gershman, D. J., Zurbuchen, T. H., Fisk, L. A., Gilbert, J. A., Raines, J. M., Anderson, B. J., Smith, C. W., Korth, H. & Solomon, S. C. (2012). Solar wind alpha particles and heavyions in the inner heliosphere. *Journal of Geophysical Research*, *117*, A00M02. https://doi.org/10.1029/2012JA017829

Glassmeier, K.-H., Grosser, J., Auster, U., Constantinescu, D., Narita, Y., & Stellmach, S. (2007). Electromagnetic induction effects and dynamo action in the Hermean system. *Space Science Reviews*, *132*(2-4), 511–527. https://doi.org/10.1007/s11214-007-9244-9

Hasegawa, H., Wang, J., Dunlop, M. W., Pu, Z. Y., Zhang, Q.-H., Lavraud, B., et al. (2010). Evidence for a flux transfer event generated by multiple X-line reconnection at the magnetopause. *Geophysical Research Letters*, *37*, L16101. https://doi.org/10.1029/2010GL044219

Heyner, D., Nabert, C., Liebert, E., & Glassmeier, K.-H. (2016). Concerning reconnection-induction balance at the magnetopause of Mercury. *Journal of Geophysical Research: Space Physics*, *121*, 2935–2961. https://doi.org/10.1002/2015JA021484

Holzer, R. E., & Slavin, J. A. (1978). Magnetic flux transfer associated with expansions and contractions of the dayside magnetosphere. *Journal of Geophysical Research*, *83*(A8), 3831. https://doi.org/10.1029/JA083iA08p03831

Hood, L., & Schubert, G. (1979). Inhibition of solar wind impingement on Mercury by planetary induction currents. *Journal of Geophysical Research*, *84*(A6), 2641–2647. https://doi.org/10.1029/JA084iA06p02641

Imber, S. M., Slavin, J. A., Boardsen, S. A., Anderson, B. J., Korth, H., McNutt, R. L. Jr., & Solomon, S. C. (2014). MESSENGER observations of large dayside flux transfer events: Do they drive Mercury's substorm cycle? *Journal of Geophysical Research: Space Physics*, *119*, 5613–5623. https://doi.org/10.1002/2014JA019884

Imber, S. M., & Slavin, J. A. (2017). MESSENGER observations of magnetotail loading and unloading: Implications for substorms at Mercury. *Journal of Geophysical Research: Space Physics*, *122*, 11,402–11,412. https://doi.org/10.1002/2017JA024332

Janhunen, P., & Kallio, E. (2004). Surface conductivity of Mercury provides current closure and may affect magnetospheric symmetry. *Annals of Geophysics*, *22*(5), 1829–1837. https://doi.org/10.5194/angeo-22-1829-2004

Jasinski, J. M., Slavin, J. A., Raines, J. M., & DiBraccio, G. A. (2017). Mercury's solar wind interaction as characterized by magnetospheric plasma mantle observations with MESSENGER. *Journal of Geophysical Research: Space Physics*, *122*, 12,153–12,169. https://doi.org/10.1002/2017JA024594

Jia, X., Slavin, J. A., Gombosi, T. I., Daldorff, L. K. S., Toth, G., & van der Holst, B. (2015). Global MHD simulations of Mercury's magnetosphere with coupled planetary interior: Induction effect of the planetary conducting core on the global interaction. *Journal of Geophysical Research: Space Physics*, *120*, 4763–4775. https://doi.org/10.1002/2015JA021143

Jia, X., Slavin, J. A., Poh, G., DiBraccio, G. A., Toth, G., Chen, Y., et al. (2019). MESSENGER observations and global simulations of highly compressed magnetosphere events at Mercury. *Journal of Geophysical Research: Space Physics*, *124*, 229–247. https://doi.org/10.1029/2018JA026166

Johnson, C. L., Philpott, L. C., Anderson, B. J., Korth, H., Hauck, S. A. II, Heyner, D., et al. (2016). Messenger Observations Of Induced Magnetic Fields In Mercury's Core. *Geophysical Research Letters*, *43*, 2436–2444. https://doi.org/10.1002/2015GL067370

Johnson, C. L., Purucker, M. E., Korth, H., Anderson, B. J., Winslow, R. M., Al Asad, M. M. H., et al. (2012). MESSENGER observations of Mercury's magnetic field structure. *Journal of Geophysical Research*, *117*, E00L14. https://doi.org/10.1029/2012JE004217

Kabin, K., Gombosi, T. I., DeZeeuw, D. L., & Powell, K. G. (2000). Interaction of Mercury with the solar wind. *Icarus*, *143*(2), 397–406. https://doi.org/10.1006/icar.1999.6252

Kidder, A., Winglee, R. M., & Harnett, E. M. (2008). Erosion of the dayside magnetosphere at Mercury in association with ion outflows and flux rope generation. *Journal of Geophysical Research*, *113*, A09223. https://doi.org/10.1029/2008JA013038

Killen, R. M., Burger, M. H., Vervack, R. J. Jr., & Cassidy, T. A. (2019). Understanding Mercury's Exosphere: Models derived from MESSENGER observations, Mercury. In S. C. L. R. Nittler, & B. J. Anderson (Eds.), *The View After MESSENGER*. London (Chapter 15, pp. 407–429). ISBN: 978-1107154452

Koth, H., Anderson, B. J., Johnson, C. L., Slavin, J. A., Raines, J. M., & Zurbuchen, T. H. (2019). Structure and configuration of Mercury's magnetosphere. In S. C. L. R. Nittler, & B. J. Anderson (Eds.), *Mercury: The view after MESSENGER* (Chapter 16 430–460). London: Cambridge Univ. Press.

Lee, L. C. & Fu, Z. F. (1985). A theory of magnetic flux transfer at theEarth's magnetopause. *Geophysical Research Letters*, *12*, 105–108.

Liljeblad, E., Karlsson, T., Raines, J. M., Slavin, J. A., Kullen, A., Sundberg, T., & Zurbuchen, T. H. (2015). MESSENGER observations of the dayside low-latitude boundary layer in Mercury's magnetosphere. *Journal of Geophysical Research: Space Physics*, *120*, 8387–8400. https://doi.org/10.1002/2015JA021662

Massetti, S., Orsini, S., Milillo, A., Mura, A., deAngelis, E., Lammer, H., & Wurz, P. (2003). Mapping of the cusp plasma precipitation on the surface of Mercury. *Icarus*, *166*(2), 229–237. https://doi.org/10.1016/j.icarus.2003.08.005

Muller, J., Simon, S., Wang, Y.-C., Motschmann, U., Heyner, D., Schüle, J., et al. (2012). Origin of Mercury's double magnetopause: 3D hybrid simulation with A.I.K.E.F. *Icarus*, *218*(1), 666–687. https://doi.org/10.1016/j.icarus.2011.12.028

Ness, N. F., Behannon, K. W., Lepping, R. P., Whang, Y. C., & Schatten, K. H. (1974). Magnetic field observations near Mercury: Preliminary results from Mariner 10. *Science*, *185*(4146), 151–160. https://doi.org/10.1126/science.185.4146.151

Odstrcil, D., Riley, P., & Zhao, X. P. (2004). Numerical simulation of the 12 May 1997 interplanetary CME event. *Journal of Geophysical Research*, *109*, A02116. https://doi.org/10.1029/2003JA010135

Ogilvie, K. W., Scudder, J. D., Vasyliunas, V. M., Hartle, R. E., & Siscoe, G. L. (1977). Observations at the planet Mercury by the plasma electron experiment, Mariner 10. *Journal of Geophysical Research*, *82*(13), 1807–1824. https://doi.org/10.1029/JA082i013p01807

Paschmann, G., Papamastorakis, I., Baumjohann, W., Carlson, B. U., Lühr, H., Sckope, N. W., & Sonnerup, O. (1986). The magnetopause for large magnetic shear: AMPTE/IRM observations. *Journal of Geophysical Research*, *91*(A10), 11,099–11,115. https://doi.org/10.1029/JA091iA10p11099

Pfleger, M., Lichtenegger, H. I. M., Wurtz, P., Lammer, H., Kallio, E., Alho, M., et al. (2015). 3D-modeling of Mercury's solar wind sputtered surface-exosphere environment. *Planetary and Space Science*, *115*, 90–101. https://doi.org/10.1016/j.pss.2015.04.016

Poh, G., Slavin, J. A., Jia, X., DiBraccio, G. A., Raines, J. M., Imber, S. M., et al. (2016). MESSENGER observations of cusp plasma filaments at Mercury. *Journal of Geophysical Research: Space Physics*, *121*, 8260–8285. https://doi.org/10.1002/2016JA022552

Raeder, J. (2006). Flux transfer events: 1. Generation mechanism for strong southward IMF. *Annals of Geophysics*, *24*(1), 381–392. https://doi.org/10.5194/angeo-24-381-2006

Raines, J. M., DiBraccio, G. A., Cassidy, T. A., Delcourt, D. C., Fujimoto, M., Jia, X., et al. (2015). Plasma sources in planetary magnetospheres: Mercury. *Space Science Reviews*, *192*(1-4), 91–144. https://doi.org/10.1007/s11214-015-0193-4

Raines, J. M., Gershman, D. J., Slavin, J. A., Zurbuchen, T. H., Korth, H., Anderson, B. J., & Solomon, S. C. (2014). Structure and dynamics of Mercury's magnetospheric cusp: MESSENGER measurements of protons and planetary ions. *Journal of Geophysical Research: Space Physics*, *119*, 6587–6602. https://doi.org/10.1002/2014JA020120

Raines, J. M., Slavin, J. A., Zurbuchen, T. H. Gloeckler, G., Anderson, B. J., Baker, D. N., et al. (2011). MESSENGER observations of the plasma environment near Mercury. *Planet. Space Sci.*, *59*,2004–2015. https://doi.org/10.1016/j/pss.2011.02.004

Rijnbeek, R. P., Cowley, S. W. H., Southwood, D. J., & Russell, C. T. (1984). A survey of dayside flux transfer events observed by ISEE-1 and ISEE-2 magnetometers. *Journal of Geophysical Research*, *89*(A2), 786–800. https://doi.org/10.1029/JA89iA02p00786

Russell, C. T., & Elphic, R. C. (1978). Initial ISEE magnetometer results: Magnetopause observations. *Space Science Reviews*, *22*(6), 681–715. https://doi.org/10.1007/BF00212619

Shue, J. -H., Chao, J. K., Fu, H. C., Russell, C. T., Song, P., Khurana, K. K., & Singer, H. J. (1997). A new functional form to study the solar wind control of the magnetopause size and shape. *Journal of Geophysical Research*, *102*(A5), 9497–9511. https://doi.org/10.1029/97JA00196

Siscoe, G., & Christopher, L. (1975). Variations in the solar wind stand-off distance at Mercury. *Geophysical Research Letters*, *2*(4), 158–160. https://doi.org/10.1029/GL002i004p00158

Slavin, J. A., Anderson, B. J., Baker, D. N., Benna, M., Boardsen, S. A., Gloeckler, G., et al. (2010). MESSENGER observations of extreme loading and unloading of Mercury's magnetic tail. *Science*, *329*(5992), 665–668. https://doi.org/10.1126/science.1188067

Slavin, J. A., Anderson, B. J., Zurbuchen, T. H., Baker, D. N., Krimigis, S. M., Acuña, M. H., et al. (2009). MESSENGER observations of Mercury's magnetosphere during northward IMF. *Geophysical Research Letters*, *36*, L02101. https://doi.org/10.1029/2008GL036158

Slavin, J. A., Baker, D. N., Gershman, D. J., Ho, G., Imber, S. M., Krimigis, S. M., & Sundberg, T. (2019). Mercury's dynamic magnetosphere. In S. C. L. R. Nittler, & B. J. Anderson (Eds.), *Mercury: The view after MESSENGER* (Chapter 17, pp. 461–496). London: Cambridge Univ. Press. ISBN: 978-1107154452

Slavin, J. A., DiBraccio, G. A., Gershman, D. J., Imber, S., Poh, G. K., Raines, J., et al. (2014). MESSENGER observations of Mercury's dayside magnetosphere under extreme solar wind conditions. *Journal of Geophysical Research: Space Physics*, *119*, 8087–8116. https://doi.org/10.1002/2014JA020319

Slavin, J. A., Elphic, R. C., Russell, C. T., Scarf, F. L., Wolfe, J. H., Mihalov, J. D., et al. (1980). The solar wind interaction with Venus: Pioneer Venus Observations of bow shock location and structure. *Journal of Geophysical Research*, *85*(A13), 7625. https://doi.org/10.1029/JA085iA13p07625

Slavin, J. A., Fairfield, D. H., Lepping, R. P., Szabo, A., Reiner, M. J., Kaiser, M., et al. (1997). WIND, Geotail and GOES 9 observations of magnetic field dipolarization and bursty bulk flows in the near-tail. *Geophysical Research Letters*, *24*(8), 971–974. https://doi.org/10.1029/97GL00542

Slavin, J. A., & Holzer, R. E. (1979). The effect of erosion on the solar wind stand-off distance at Mercury. *Journal of Geophysical Research*, *84*(A5), 2076–2,082. https://doi.org/10.1029/JA084iA05p02076

Slavin, J. A., & Holzer, R. E. (1981). Solar wind flow about the terrestrial planets, 1. Modeling bow shock position and shape. *Journal of Geophysical Research*, *86*(A13), 11401–11,418. https://doi.org/10.1029/JA086iA13p11401

Slavin, J. A., Imber, S. M., Boardsen, S. A., DiBraccio, G. A., Sundberg, T., Sarantos, M., et al. (2012). MESSENGER observations of a flux transfer shower at Mercury. *Journal of Geophysical Research*, *117*, A00M06. https://doi.org/10.1029/2012JA017926

Slavin, J. A., Smith, E. J., Sibeck, D. G., Baker, D. N., Zwickl, R. D., & Akasofu, S.-I. (1985). An ISEE-3 study of average and substorm conditions in the distant magnetotail. *Journal of Geophysical Research*, *90*(A11), 10,875–10,895. https://doi.org/10.1029/JA090iA11p10875

Smith, D. E., Zuber, M. T., Phillips, R. J., Solomon, S. C., Hauck, S. A. II, Lemoine, F. G., et al. (2012). Gravity field and internal structure of Mercury from MESSENGER. *Science*, *336*(6078), 214–217. https://doi.org/10.1126/science.1218809

Solomon, S. C., McNutt, R. L. Jr., Gold, R. E., & Domingue, D. L. (2007). MESSENGER mission overview. *Space Science Reviews*, *131*(1-4), 3–39. https://doi.org/10.1007/s11214-007-9247-6

Sonnerup, B. U. Ö. (1974). Magnetopause reconnection rate. *Journal of Geophysical Research*, *79*, 1546–1549, https://doi.org/10.1029/JA079i010p01546

Sonnerup, B. U. Ö., Papmastorakis, I., Paschmann, G., & Lühr, H. (1990). The magnetopause for large magnetic shear: Analysis of convection electric fields from AMPTE/IRM. *Journal of Geophysical Research*, *95*, 10,541–10,557. https://doi.org/10.1029/JA095iA07p10541

Spreiter, J. R., Summers, A. L., & Alksne, A. Y. (1966). Hydromagnetic flow around the magnetosphere. *Planetary and Space Science*, *14*, 223–253. https://doi.org/10.1016/0032-0633(66)90124-3

Suess, S. T., & Goldstein, B. E. (1979). Compression of the Hermaean magnetosphere by the solar wind. *Journal of Geophysical Research*, *84*(A7), 3306–3312. https://doi.org/10.1029/JA084iA07p03306

Tanskanen, E. I. (2009). A comprehensive high-throughput analysis of substorms observed by IMAGE magnetometer network: Years 1993–2003 examined. *Journal of Geophysical Research*, *114*, A05204. https://doi.org/10.1029/2008JA013682

Toth, G., & Odstrcil, D. (1996). Comparison of some flux corrected transport and total variation diminishing numerical schemes for hydrodynamic and magnetohydrodynamic problems. *Journal of Computational Physics*, *128*(1), 82–100. https://doi.org/10.1006/jcph.1996.0197

Trávníček, P. M., Hellinger, P., Schriver, D., Herčík, D., Slavin, J. A., & Anderson, B. J. (2009). Kinetic instabilities in Mercury's magnetosphere: Three-dimensional simulation results. *Geophysical Research Letters*, *36*, L07104. https://doi.org/10.1029/2008GL036630

Trávníček, P. M., Schriver, D., Hellinger, P., Herčík, D., Anderson, B. J., Sarantos, M., & Slavin, J. A. (2010). Mercury's magnetosphere–solar wind interaction for northward and southward interplanetary magnetic field: Hybrid simulations. *Icarus*, *209*(1), 11–22. https://doi.org/10.1016/j.icarus.2010.01.008

Trenchi, L., Marcucci, M. F., Rème, H., Carr, C. M., & Cao, J. B. (2011). TC-1 observations of a flux rope: Generation by multiple X line reconnection. *Geophysical Research Letters*, *116*, A05202. https://doi.org/10.1029/2010JA015986

Varela, J., Pantellini, F., & Moncuquet, M. (2015). The effect of interplanetary magnetic field orientation on the solar wind flux impacting Mercury's surface. *Planetary and Space Science*, *119*, 264–269. https://doi.org/10.1016/l.pss.2015.10.004

Wang, Y. C., Motschmann, U., Müller, J., & Ip, W. H. (2010). A hybrid simulation of Mercury's magnetosphere for the MESSENGER encounters in year 2008. *Icarus*, *209*, 46–52.

Webster, J. M., Burch, J. L., Reiff, P. H., Daou, A. G., Genestreti, K. J., Graham, D. B., et al. (2018). Magnetospheric Multiscale dayside reconnection electron diffusion region events. *Journal of Geophysical Research: Space Physics*, *123*, 4858–4878. https://doi.org/10.1029/2018JA025245

Winslow, R. M., Anderson, B. J., Johnson, C. L., Slavin, J. A., Korth, H., Purucker, M. E., et al. (2013). Mercury's magnetopause and bow shock from MESSENGER observations. *Journal of Geophysical Research: Space Physics*, *118*, 2213–2227. https://doi.org/10.1002/jgra.50237

Winslow, R. M., Johnson, C. L., Anderson, B. J., Korth, H., Slavin, J. A., Purucker, M. E., & Solomon, S. C. (2012). Observations of Mercury's northern cusp region with MESSENGER's Magnetometer. *Geophysical Research Letters*, *39*, L08112. https://doi.org/10.1029/2012GL051472

Winslow, R. M., N. Lugaz, C. J. Farrugia, C. L. Johnson, B. J. Anderson, C. S. Paty, et al., First observations of an ICME compressing Mercury's dayside magnetosphere to the surface, arXiv:1903.00577v1 (2019).

Winslow, R. M., Winslow, R. M., Lugaz, N., Philpott, L. C., Schwadron, N. A., Farrugia, C. J., et al. (2015). Interplanetary coronal mass ejections from MESSENGER orbital observations at Mercury. *Journal of Geophysical Research: Space Physics*, *120*, 6101–6118. https://doi.org/10.1002/2015JA021200

Zhong, J., Wan, W. X., Slavin, J. A., Wei, Y., Lin, R. L., Chai, L. H., et al. (2015). Mercury's three-dimensional asymmetric magnetopause. *Journal of Geophysical Research: Space Physics*, *120*, 7658–7671. https://doi.org/10.1002/2015JA021425

Zhong, J., Wan, W. X., Wei, Y., Slavin, J. A., Raines, J. M., Rong, Z. J., et al. (2015). Compressibility of Mercury's dayside magnetosphere. *Geophysical Research Letters*, *42*, 10,135–10,139. https://doi.org/10.1002/2015GL067063

Zong, Q.-G., Fritz, T. A., Spence, H., Zhang, H., Huang, Z. Y., Pu, Z. Y., et al. (2005). Plasmoid in the high latitude boundary/cusp region observed by Cluster. *Geophysical Research Letters*, *32*, L01101. https://doi.org/10.1029/2004GL020960

Zwan, B. J. & Wolf, R. A. (1976). Depletion of solar wind plasmanear a planetary boundary. *Journal of Geophysical Research*, *81*, 1636–1648. https://doi.org/10.1029/JA081i010p01636